A few upstream bifurcations drive the spatial distribution of red blood cells in model microfluidic networks

Adlan Merlo, Maxime Berg, Paul Duru, Frédéric Risso, Yohan Davit, Sylvie Lorthois

To cite this version:

Adlan Merlo, Maxime Berg, Paul Duru, Frédéric Risso, Yohan Davit, et al.. A few upstream bifurcations drive the spatial distribution of red blood cells in model microfluidic networks. Soft Matter, 2022, 18 (7), pp.1463-1478. 10.1039/d1sm01141c . hal-03797095

Soft Matter

ARTICLE TYPE

Cite this: DOI: 00.0000/xxxxxxxxxx

Received Date
Accepted Date

DOI: 00.0000/xxxxxxxxxx

A few upstream bifurcations drive the spatial distribution of red blood cells in model microfluidic networks

Adlan Merlo,[‡] Maxime Berg,[‡] Paul Duru, Frédéric Risso, Yohan Davit, and Sylvie Lorthois[a]

The physics of blood flow in small vessel networks is dominated by the interactions between Red Blood Cells (RBCs), plasma and blood vessel walls. The resulting couplings between the microvessel network architecture and the heterogeneous distribution of RBCs at network-scale are still poorly understood. The main goal of this paper is to elucidate how a local effect, such as RBC partitioning at individual bifurcations, interacts with the global structure of the flow field to induce specific preferential locations of RBCs in model microfluidic network. First, using experimental results, we demonstrate that persistent perturbations to the established hematocrit profile after diverging bifurcations may bias RBC partitioning at the next bifurcations. By performing a sensitivity analysis based upon network models of RBC flow, we show that these perturbations may propagate from bifurcation to bifurcation, leading to an outsized impact of a few crucial upstream bifurcations on the distribution of RBCs at network-scale. Based on measured hematocrit profiles, we further construct a modified RBC partitioning model that accounts for the incomplete relaxation of RBCs at these bifurcations. This model allows us to explain how the flow field results in a single pattern of RBC preferential location in some networks, while it leads to the emergence of two different patterns of RBC preferential location in others. Our findings have important implications in understanding and modeling blood flow in physiological and pathological conditions.

1 Introduction

Microvascular networks are able to ensure adequate blood supply, feeding every cell in peripheral tissues with oxygen and nutrients under a wide range of physiological conditions and for varying metabolic needs. In the bloodstream, oxygen is mostly bound to hemoglobin inside Red Blood Cells (RBCs) and is progressively released to feed the tissues. Transport of oxygen throughout the microvascular network and tissue oxygenation therefore strongly depend on the transport of RBCs. The distribution of RBCs in microvascular networks, however, is highly heterogeneous, with vessels only containing suspending fluid (plasma) and others that are almost completely crowded with RBCs[1–4]. Understanding how the heterogeneous distribution of RBCs is driven by the microvascular architecture is thus an important step towards developing new generations of oxygen transport models at the tissue-scale, which may be key in elucidating a large range of pathologies, from cancers[5] to Alzheimer's disease[6,7].

Schematically, the problem is that of confined deformable RBCs being transported by plasma through complex microvessel networks, with vessel diameters of the same order as RBCs. In such networks, the physics of blood flow is dominated by the interactions between RBCs, plasma and blood vessel walls[8]. In each vessel, wall-induced migration drives RBCs away from the walls and shear-induced diffusion due to collisions between RBCs partly counteracts this effect. This competition simultaneously results in RBC enrichment in a relatively large region in the center of the vessel and in the formation of a depletion layer near the walls, also known as the cell-free layer[9,10]. The resulting RBC radial distribution at vessel-scale plays a fundamental role in determining how RBCs distribute at bifurcations. The cell-free layer often preferentially feeds one daughter branch and the enriched region the other daughter branch[10,11], leading to an inhomogeneous distribution of RBCs downstream diverging bifurcations. This phenomenon, known as the phase separation effect, is the main local mechanism leading to RBC heterogeneities at network-scale. Because of its local nature, phase separation strongly depends on the local geometry of the bifurcation, in particular the diameter of each branch relatively to the size of RBCs and to the diameter of the other branches[12]. Phase separation at a given bifurcation is also affected by the global architecture of the network. Flow, for instance, is a strong driver that is not determined locally. For a given flow rate in the feeding branch, the distribution of flow in

---

Institut de Mécanique des Fluides de Toulouse, IMFT, Université de Toulouse, CNRS, Toulouse, France

‡ These authors contributed equally to this work.

[a] Corresponding author (sylvie.lorthois@imft.fr).

each daughter branch depends on both their relative conductivity and the conductivity of the network downstream. Similarly, the volume fraction of RBCs (tube hematocrit) in each vessel is the result of a transport problem over the entire network[12–16].

Any mechanism that disturbs the cell free layer, modifying the RBC distribution in the feeding branch, or that distorts the flow-field, modifying the shape of the separation surface between the two daughter branches, may impact phase separation. An example of a mechanism that distorts the cell free layer is the relaxation of RBCs after a bifurcation. If two successive bifurcations are sufficiently close, RBCs will not have enough time to reach their established radial position in the connecting vessel, and phase separation will be altered in the downstream bifurcation, as already noted in[12,17] and recently confirmed by[16,18–20]. In the case of a bifurcation with daughter branches of equal diameter, this may result in the RBC enrichment of the low flow branch[12,16–20] and lead to a situation that is qualitatively similar to the case with daughter branches of unequal diameters, where the low-flow branch preferentially receives blood from the enriched central region[12,21].

Predicting the distribution of RBCs in interconnected networks, even the simplest ones, has thus proven highly challenging. Fig. 1 shows an example of a microfluidic experiment of RBC transport through a square network with a single inlet and a single outlet located in opposite corners. Using this model system, we observed unexpected differences of the RBC distributions, depending on the width of the channels. For the largest channels, with square cross-sections of $10 \times 10 \mu m^2$, RBCs preferentially flow through the central region of the network (Fig. 1, left panel). This yields a positive correlation between the tube hematocrit and the flow velocity in individual channels, consistent with the so-called tissue Fåhraeus effect†[22,23]. For thinner channels with square cross-sections of $5 \times 5 \mu m^2$, the RBC pattern is radically different. RBCs accumulate in the top left (red box in Fig. 1b) and bottom right corners, with relatively less RBCs in the central region (blue box in this same figure), resulting in a negative correlation between RBC concentration and velocity. This latter distribution had been theoretically predicted based on a simple Lagrangian network model of RBC flow within networks[24], but had never been confirmed experimentally before.

One possible explanation for these differences could be that they result from flow perturbations caused by the presence of RBCs. In fact, in the absence of RBCs, the velocity fields in both networks are identical when normalized by the inlet velocity. For the small inlet tube hematocrit considered here ($H_t^i = 0.05$), the perturbation of the flow field induced by the presence of RBCs is a second-order effect. Such an effect cannot drive a reversal of the flow partitioning at any bifurcation. It can even less induce a reversal of the branch with the highest RBC fraction as an increased RBC fraction in a given branch would increase viscous dissipation, re-balancing the flow and thus the RBCs toward the other branch[19,24,25]. Therefore, the different patterns observed experimentally cannot be explained by RBC-associated flow perturbations.

What, then, is driving the distribution of RBCs through the network? To address this question, we combine microfluidic experiments with network modeling, focusing on both square networks with a four-neighbor connectivity and hexagonal networks (Fig. 2) with a three-neighbor connectivity. In both configurations, we show that with narrow channels, or equivalently with wide channels and high concentrations of RBCs, the radial RBC profiles relax rapidly between bifurcations and the distribution of RBCs through the networks is consistent with that predicted by models based on established distributions. For wider channels with lower concentrations of RBCs, however, we show that the radial RBC profiles do not have time to relax between bifurcations, hence modifying phase separation and altering the overall distribution of RBCs through the network. This effect preferentially occurs near the inlet and then propagates through the network, leading to an outsized impact of a few key upstream bifurcations on the RBC distribution at network-scale. In particular, we show that, for strikingly different RBC organizations to emerge, as observed in square networks (Fig. 1), incomplete relaxation must bias RBCs toward the branches which receive the lowest flow fraction at these bifurcations. Overall, we thus demonstrate that the distribution of RBCs in these different networks results from a subtle interplay between the global network architecture and the local physics of phase separation at successive bifurcations.

For that purpose, in Section 2, we first study hexagonal networks with a three-neighbor connectivity that mimics the topology of real microvascular networks (see e.g.[26,27]) and has been studied extensively[12,14,18,19]. The corresponding model of phase separation, in the standard case whereby the vessels are sufficiently long to enable RBC relaxation, is well-established and empirical parametric descriptions have been developed specifically for this case[12,15,28]. They provide quantitative reference solutions allowing to precisely pinpoint which parameters are modified by the incomplete relaxation of RBCs. They also make it possible to explore the link between local and global effects through a sensitivity analysis and to show that a few upstream bifurcations drive the RBC distribution at network-scale. In Section 3, we then use this knowledge to elucidate how these few upstream bifurcations lead to the emergence of strikingly different RBC organizations in square networks, explaining why a positive correlation may be generally expected between high velocity and high hematocrit vessels. We then summarize our findings in Section 4 and discuss their relevance in physiology or pathology in Section 5.

2 Results in hexagonal networks

In this Section, we first present the results of microfluidic experiments, in which we flow dilute human RBCs ($H_t^i = 0.035$) through hexagonal polydimethylsiloxane (PDMS)-glass networks (Fig. 2a,b), as detailed in the Materials and Methods (Section 6.1). These networks are made of $50 \mu m$ long channels of square cross-sections $10 \times 10 \mu m^2$. We study the heterogeneous

---

† The tissue Fåhraeus effect denotes a reduction of the volume fraction of RBCs in the whole network by comparison to its discharge hematocrit (defined as the ratio between the RBC flow and the total flow)[22,23]. It is analogous to the Fåhraeus effect, *i.e.*, the reduction of the hematocrit within a single segment (tube hematocrit) by comparison to the discharge hematocrit, which results from the correlation between hematocrit and velocity within a single vessel cross-section[12].

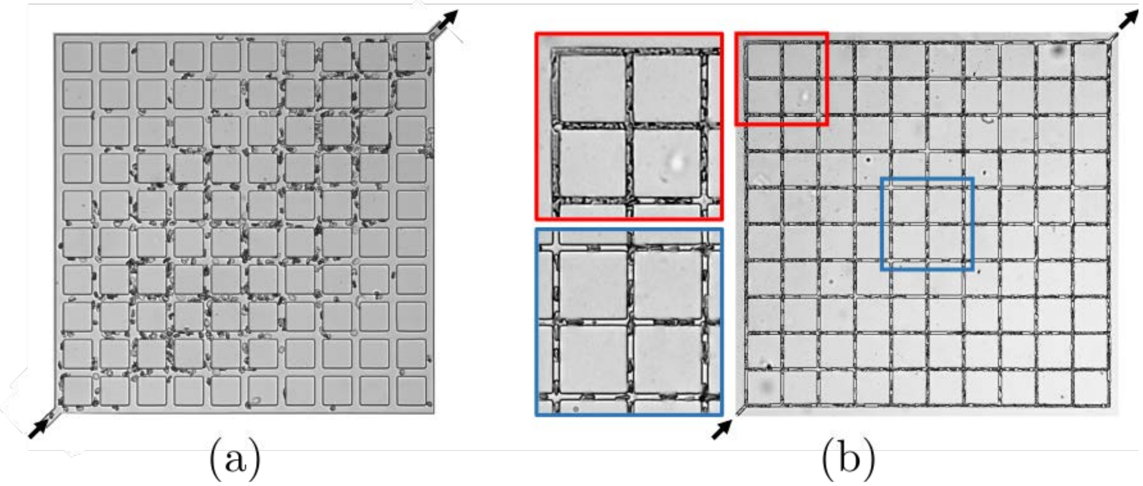

Figure 1 Instantaneous snapshots of red blood cell distribution in a square network ($50\ \mu m$-long channels, $H_t \approx 0.05$). The flow is from the lower left corner to the upper right corner. (a): $10\mu m$-side channels (b): $5\mu m$-side channels. Enlarged views of central and corner areas are displayed in blue and red, respectively.

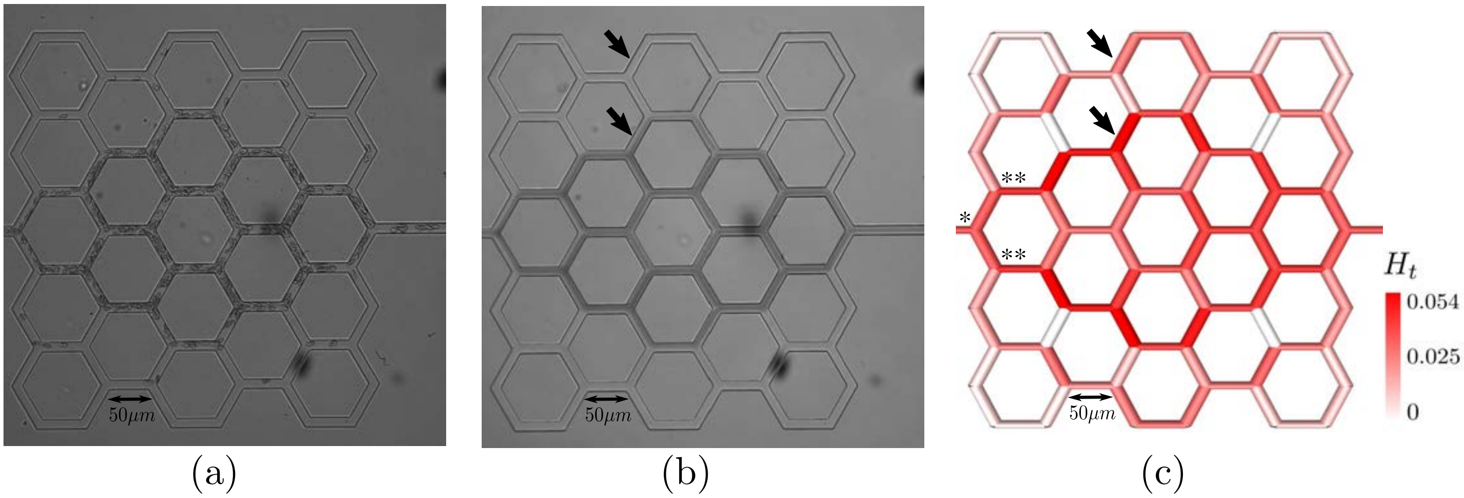

Figure 2 Red blood cell distribution in a hexagonal network with $50\mu m$ long channels of square cross-sections $10 \times 10\mu m^2$. The flow is from left to right, with an inlet tube hematocrit of $H_t^i = 0.035$. (a): Instantaneous snapshot (intensity I in grey levels). (b): Time-averaged intensity field (averaged over 3s). (c): *In silico* predictions of stationary tube hematocrit obtained using the equivalent fluid model presented in Section 6.2. The first bifurcation and the second bifurcations of the network are respectively labelled by $*$ and $**$. Arrows in (b) and (c) point towards two channels exhibiting significant discrepancies between experiment and simulations.

distribution of RBCs at network-scale (Section 2.1), quantifying differences from channel to channel by optical microscopy, as described in Section 6.1. We compare our experimental results to the predictions of the classical non-linear equivalent fluid network model of blood flow, which is described in Section 6.2. This model describes the blood as an equivalent single-phase fluid and uses phenomenological descriptions to account for the complex rheological properties of blood in the microcirculation, including the Fåhraeus, Fåhraeus-Lindqvist and phase-separation effects. By modifying different parameters in these phenomenological descriptions and by performing sensitivity analyses in the model, we assess the relevance of various hypotheses regarding the interplay between the network architecture and the local physics of phase separation and their relative influence on the RBC distribution.

2.1 Red blood cell heterogeneities at network-scale

The RBC spatial distribution observed in our experiments (Fig. 2a and b) is in qualitative agreement with recent results obtained in similar networks with a larger number of channels[19]. It shows a preferential location of the cells in the center of the network and surrounding channels almost devoid of RBCs. However, it also shows strong discrepancies with the predictions of the classical non-linear network model of blood flow (Fig. 2c) detailed in Section 6.2. This model also leads to an enrichment of the network center compared to the periphery, which is due to the velocity distribution in the branches downstream the second bifurcations (labeled by $**$ in Fig. 2c). At these bifurcations, the theoretical flow fraction entering the peripheral branches is 36.7% at baseline, i.e. without any RBC. Phase separation thus leads to RBC depletion in the network periphery. However, this model globally underestimates spatial heterogeneities throughout the network and results in some peripheral channels having the same hematocrit as some central channels (see channels labeled by arrows in Fig. 2c).

These differences are confirmed quantitatively by comparing, for all channels in the network, the predicted tube hematocrit to the measured one (red circles in Fig. 3a). In a significant number of channels, not a single RBC has been observed for the whole duration of the experiment and $H_{t,\exp}$ equals 0. The model, however, predicts a hematocrit equal to the inlet value in these same channels. For all other channels, the hematocrit range predicted by the model ($\sim$ 0.03 to 0.06) is narrower than the measured one ($\sim$ 0.03 to 0.08). These discrepancies lead to a poor correlation between the predicted and measured hematocrit, with a Pearson's correlation coefficient $r < 0.8$ and a slope m far from unity ($m \simeq 0.4$). By contrast, the predicted RBC velocities, normalized by the RBC velocity in the inlet branch, are in very good agreement with the measured velocities (red circles in Fig. 3b), with $r = 0.99$ and $m = 0.97$.

The above results still hold if the viscous dissipation induced by the RBCs is neglected (blue crosses in Figs. 3a and 3b). Indeed, if the viscosity is kept constant, neither the hematocrit nor the normalized velocity fields are significantly modified. The impact of the viscous dissipation induced by RBCs at channel-scale is therefore negligible for the small hematocrits considered here. In other words, the results of the model have little sensitivity to the description of the Fåraeus-Lindqvist effect so that we can rule out this effect as being the source of discrepancy between the experimental and predicted hematocrit fields (Fig. 3a).

Several other phenomena could explain this discrepancy. It could be due to the non-uniqueness of the solution of the mathematical equations describing the flow. The blood flow problem detailed in Section 6.2.1 forms a nonlinear problem, which could lead to the emergence of multiple equilibria[29,30]. If that happened, the simulation would be very sensitive to all aspects of the numerical scheme and our approach may capture the wrong solution. We have tested this hypothesis using the resolution procedure described in Supplementary Information SIA and, by contrast to the ladder network shown in Fig. SI1, we did not obtain more than one solution. Thus, it is likely that the simulated hematocrit solution corresponds to what is observed in experiments. The last possibility would be that there is an important physical process that is not captured by the model. We have shown in[14] that, for the channel size and hematocrit considered here, the phase separation effect observed at individual microfluidic bifurcations is qualitatively and quantitatively well described by the empirical set of relations deduced from *in vivo* experiments. However, these microfluidic experiments were performed for a single bifurcation with a long straight entry branch. They do not take into account the presence of the bifurcation located immediately upstream. Such a bifurcation has been shown to bias the spatial distribution of RBCs across the inlet channel of the considered bifurcation, with potentially strong impact on the downstream phase separation for a large range of channel sizes. We explore further this hypothesis in the next Sections and study how heterogeneities of RBC flow at channel-scale build up within the network through successive bifurcations.

2.2 Red blood cell heterogeneities at channel-scale

The first bifurcation of the network, labeled by $*$ in Fig. 4a, is located downstream a long and straight channel. The length is sufficient to ensure that the flow is established and has reached a steady state. Moreover, the network geometry is symmetrical around its inlet/outlet axis (i/o axis), so that the flow rates in both its daughter channels are equal. While some instantaneous asymmetries of RBC shape and position can be observed at this bifurcation (see e.g. first left cell in Fig. 4a), the time-averaged RBC concentration in grey in Fig. 4b is approximately symmetrical around the i/o axis. The hematocrit profile across the inlet channel just upstream the bifurcation is also symmetrical (Fig. 4c).

Consistent with[19,20], Fig. 4b, however, clearly indicates that RBCs are, on average, biased toward the side of the bifurcation apex in the daughter channels. This results in strong asymmetries of the hematocrit profiles that persist through the whole length of the daughter channels (Fig. 4b and d). This further increases the inequality of the RBC distribution downstream the next bifurcations, labeled by $**$ in Fig. 4a, and significantly modifies the distribution at network-scale. The same phenomenon repeats bifurcation after bifurcation. It seems likely that the impact on the global RBC distribution will depend on the hierarchical position of the bifurcation in the network. The relative importance of each bifurcation is particularly difficult to verify experimentally in interconnected networks because the local/global couplings make it impossible to manipulate phase separation at a single bifurcation. To explore this, we perform in the next Section a numerical sensitivity analysis designed to study how the topological position of a bifurcation relative to the network inlet affects the RBC distribution at network-scale.

2.3 Influence of the topological position in the network

The main idea is to rely on numerical modeling to independently manipulate the magnitude of phase separation at each divergent bifurcation. We use the same classical nonlinear network model of blood flow as the one used in Section 2.1 for the comparison with our experiments. However, here, we treat the fractional RBC (or erythrocyte) flow FQ_E, defined as the ratio of RBC flow in one of its daughter branches to the RBC flow in the feeding branch, as an independent random variable that follows a uniform distribution between 0 and 1. We then compute the resulting tube hematocrits in each segment of the network by solving the flow problem and deduce the total Sobol indices associated with these random variables, as described in the Materials and Methods (Section 6.2.3).

These total Sobol indices measure the influence of phase separation at bifurcation j on the tube hematocrit in each vessel i of the network. The total Sobol index of segment i associated with bifurcation j is equal to zero if phase separation at j has no influence on the hematocrit in i and to one if i is only influenced by j. These indices are shown in Fig. 5a where each row represents a given segment and each column a bifurcation ranked according to its order, defined as its topological distance to the first bifurca-

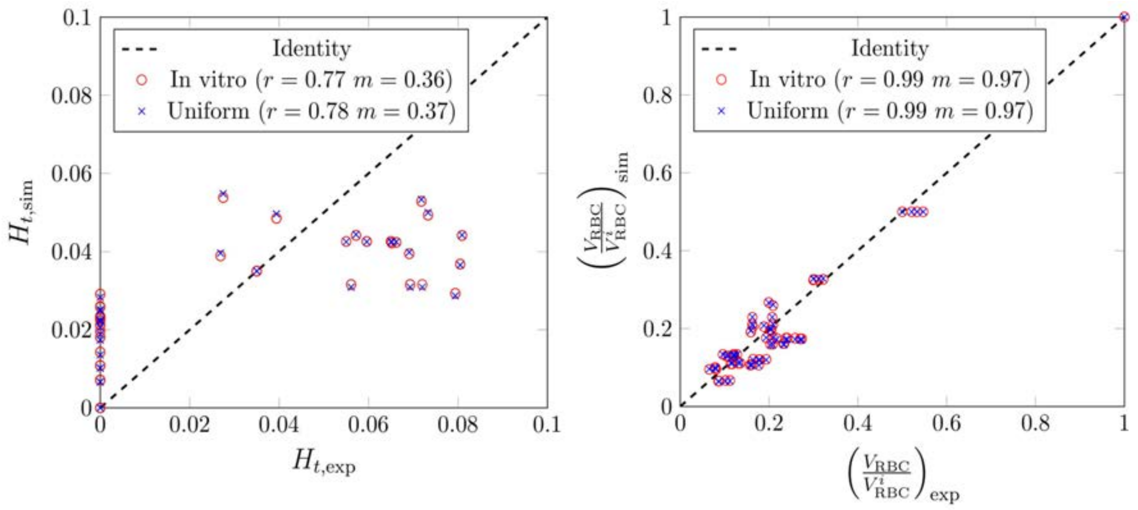

(a) (b)

Figure 3 Comparison between model and experiments for a hexagonal network with $10\mu m$-side channels. (a): segment by segment comparison between predicted and measured tube hematocrits and (b): normalized red blood cell velocity $\frac{V_{RBC}}{V^i_{RBC}}$ distributions, where V^i_{RBC} is the velocity in the network inlet branch. The effective viscosity used in the effective fluid model has little impact on the results. Blue crosses correspond to a uniform viscosity and red circles to the effective viscosity previously derived from *in vitro* experiments (Eqs. 9 to 11). For each scenario, the correlation coefficient r and the slope of the best linear fit m are given in the legend.

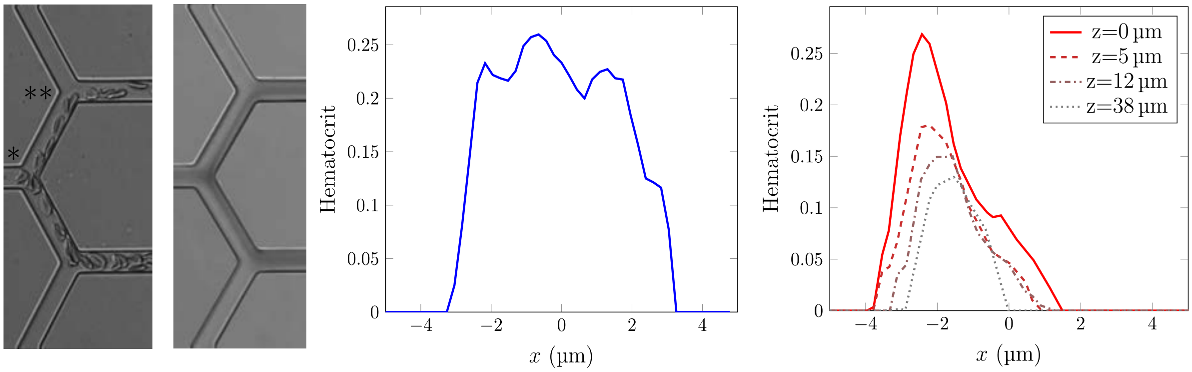

(a) (b) (c) (d)

Figure 4 The hematocrit profile exhibits strong asymmetries upon leaving the first bifurcation ($*$), which persist until the second bifurcation ($**$) in a hexagonal network with $10\mu m$-side channels. (a): Zoomed instantaneous intensity snapshot showing red blood cells flowing through the first ($*$) and second ($**$) bifurcations of the network. (b): Corresponding time-averaged intensity field. (c): Tube hematocrit profile in the inlet branch, just upstream of the first bifurcation ($*$). (d): Tube hematocrit profiles in one of the branches downstream of the first bifurcation ($*$), for different axial positions (the origin corresponds to the bifurcation apex). Note that the strong variations of the average tube hematocrit with axial position result from the Fåhraeus effect, as RBCs that have been slowed down at the bifurcation apex[16,31] re-accelerate in the channel while migrating towards the channel center.

tion. As shown in Fig. 5a, the matrix is mostly upper triangular with alternating zero and non-zero values for each diverging bifurcation, the small deviations being due to vessel labelling and the matrix being non-square. This matrix structure reflects the intuition that bifurcations closer to the inlet impact a larger number of segments because information propagates primarily in the direction of the flow. Because of the weak feedback of RBCs on the flow, variations in the hematocrit of a vessel downstream a given bifurcation do not significantly change the hematocrit of any other vessel located upstream of this bifurcation. This results in null values of the associated Sobol indices and explains why the number of non-zero values in the Sobol matrix decreases with increasing bifurcation order.

Consistently, Fig. 5a shows that the first bifurcation (order-0) has the strongest effect on the tube hematocrit of every vessel in the network, independently from their position relative to the network i/o axis, with most Sobol indices above 0.25. Order-1 bifurcations still influence all vessels located on the same side of the i/o axis, with Sobol indices up to 0.5, and on the other side when progressing downstream (Fig. 5b). As illustrated in Fig. 5c for an order-4 bifurcation, Sobol indices are not zero only for a small number of vessels, all located on the same side of the i/o axis. Moreover, Sobol indices associated with higher order bifurcations are typically smaller than those associated with order-1

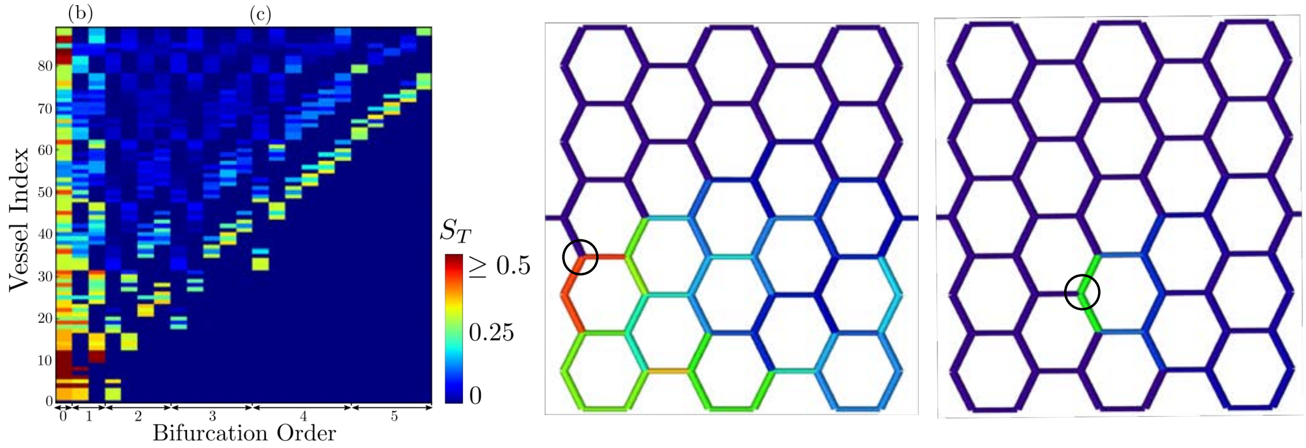

(a) (b) (c)

Figure 5 The tube hematocrit distribution is mainly sensitive to the description of phase separation in the upstream bifurcations in a hexagonal network with $10\mu m$-side channels. (a): Total Sobol index matrix. Each row i represents a segment (*e.g.* $i = 0$ is the network inlet) and each column j represents a diverging bifurcation. The color associated with each cell (i, j) displays the sensitivity of the tube hematocrit in segment i associated with variations of the phase separation effect in bifurcation j. Bifurcations are sorted according to their topological distance (*i.e.* bifurcation order) to the first bifurcation. The column labeled (b) corresponds to the order-1 bifurcation indicated by a circle in panel (b), while column labeled (c) corresponds to the order-4 bifurcation indicated by a circle in panel (c). (b): Projection of column (b) of the total Sobol index matrix, i.e. column associated with the circled bifurcation, on all network segments. (c): Projection of column (c) of the total Sobol index matrix, i.e. column associated with the circled bifurcation, on all network segments.

bifurcations and the difference between Sobol indices of consecutive bifurcations of increasing orders decreases. This can be intuitively understood as the first bifurcations in the network also correspond to a larger flux of RBCs. Due to mass conservation, the flow rate decreases steadily in the diverging part of the network, where flow divides at each successive bifurcation, before alternating between divisions and recombinations induced by network interconnections. Overall, these results suggest that phase separation at order-0 and order-1 bifurcations controls most of the RBC distribution at network-scale.

We have previously shown in single microfluidic bifurcations that the phase separation model describes well the experimental results when the upstream flow is fully established, which is the case for the order-0 bifurcation. We thus hypothesize that the discrepancies between experimental and simulation results originate primarily in order-1 bifurcations. In these bifurcations, results in Section 2.2 suggest that upstream asymmetries of the RBC profile is a major physical ingredient that is not captured by the averaged parametric model. In the next Section, we test this hypothesis by using a simple correction of the phase separation model for order-1 bifurcations and go on to check whether it is sufficient to recover the RBC distribution at network-scale.

2.4 Correcting phase separation at order-1 bifurcations

The main idea is to improve the description of phase separation at order-1 bifurcations by taking the experimentally observed upstream asymmetries into account. For that purpose, following[14], we assume that, due to the high geometric confinement, the RBC velocity profile is flat ($V(x,y) = V_0$, see Fig. 6a for axis definition), with V_0 equal to the maximum suspending fluid velocity. We consider that variations of hematocrit and velocity profiles along the channel depth, i.e. along y, can be neglected. Due to the low Reynolds number ($Re \sim 0.1$), and following[12,32,33], we further assume that plasma skimming[22] is the primary effect controlling phase separation. RBCs can be treated as point particles, i.e. volumeless, that follow the suspending fluid streamlines, so that cell screening[11,16] can be neglected. Consistently, we disregard the finite size of RBCs. We thus quantify the RBC transverse distribution through the hematocrit profile and assume that the associated, virtual, RBC separation streamline matches the flow separation streamline, as illustrated in Fig. 6a. As a result, a RBC fluid particle located on a given side of this virtual line in the entry branch feeds the daughter branch located on the same side.

While Pries et al.[12] used similar arguments to infer the shape of the hematocrit profile in the entry branch from experimental phase separation data, as illustrated in Figs. 8 to 10 of their paper, the key aspect of our approach is that we use our experimentally measured hematocrit profile to correct the values of parameters (A, B, X_0) in the phase separation model, where A captures asymmetries, B controls the intensity of the non-linearity and X_0 is a threshold value for the smallest fractional blood flow value under which no RBC will enter the vessel.

Under these assumptions, if we label α the downstream branch collecting all upstream fluid in the range $x \in [-W/2, x_{ss}]$, with x_{ss} denoting the position of the fluid separation streamline in the entry channel and W the channel width, we can deduce the fractional erythrocyte flow FQ_E^α and fractional blood flow FQ_B^α as

$$\mathrm{FQ}_E^\alpha = \frac{\int_{-W/2}^{x_{ss}} H_t^e(x) V_0 dx}{\int_{-W/2}^{W/2} H_t^e(x) V_0 dx}, \tag{1}$$

and

$$\mathrm{FQ}_B^\alpha = \frac{\int_{-W/2}^{x_{ss}} (H_t^e(x) V_0 + (1 - H_t^e(x)) V_{SF}(x)) dx}{\int_{-W/2}^{W/2} (H_t^e(x) V_0 + (1 - H_t^e(x)) V_{SF}(x)) dx}, \tag{2}$$

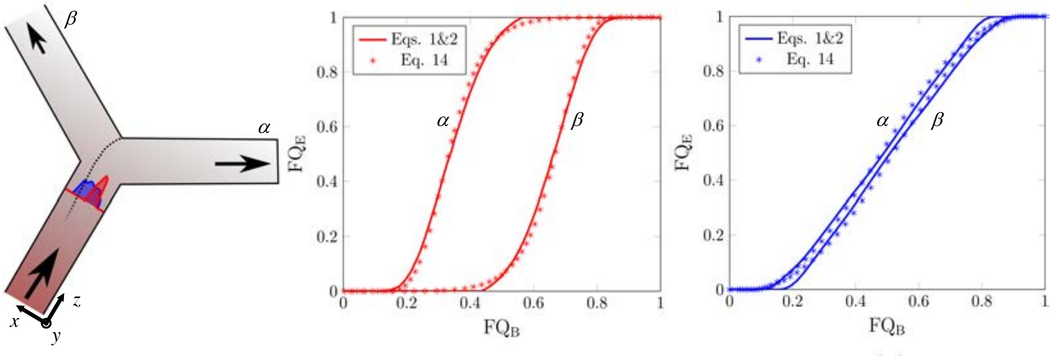

(a) (b) (c)

Figure 6 Increased phase separation induced by the asymmetry of the hematocrit profile in the upstream $10\mu m$-side channel can be described using a semi-empirical model (Eqs. 1 and 2). (a): Sketch illustrating the RBC flow distribution downstream a bifurcation for the strongly asymmetric (red) and a quasi-symmetric (blue) hematocrit profile displayed in Fig. 4. The black dotted line schematizes the virtual RBC separation streamline between the two downstream segments, α and β, for a given flow ratio, which we assume matches the flow separation streamline. (b) and (c): Fraction of red blood cell flow rate ($\mathrm{FQ_E}$) as a function of the fraction of total blood flow rate ($\mathrm{FQ_B}$), downstream the bifurcation, for the strongly asymmetric (b) and quasi-symmetric (c) hematocrit profiles, as predicted by the semi-empirical model (continuous line). Best non-linear adjustment of the semi-empirical prediction using Eq. 14 (stars). (b) $A = 2.73$, $B = 2.78$, $X_0 = 0.15$ and (c) $A = -0.12$, $B = 1.54$, $X_0 = 0.08$. Reverse phase separation ($FQ_E^\alpha > FQ_B^\alpha$) is considerably larger in (b) than in (c).

---

where the subscript e denotes the entry branch and $V_{SF}(x) = V_0(1-4x^2/W^2)$ is the suspending fluid velocity profile, as discussed in[34]. A full semi-empirical phase separation diagram is then obtained by displacing the fluid separation streamline position from wall to wall, *i.e.* varying x_{ss} from $-W/2$ to $W/2$.

The continuous lines in Fig. 6b show the phase separation diagram corresponding to the hematocrit profile measured upstream order-1 bifurcations. Because this hematocrit profile is skewed toward the side of the previous bifurcation apex (see e.g. Fig. 4b), RBCs are strongly biased toward the daughter branch located on this same side (branch α in Fig. 6a). For comparison, Fig. 6c shows the phase separation diagram obtained with the quasi-symmetric hematocrit profile measured upstream the order-0 bifurcation. While the latter exhibits the typical shape expected for symmetrical bifurcations, the former has a shape corresponding to phase separation diagrams in highly asymmetric bifurcations[12]. Thus, we can still fit (A,B,X_0) to this phase separation diagram. This yields new values for these parameters ($A^{**} = 2.73, B^{**} = 2.78, X_0^{**} = 0.15$), only valid for order-1 bifurcations, describing the present experimental results with good accuracy (dotted lines in Fig. 6b). For comparison, in the order-0 bifurcation, the parameters are: $A^* = -0.12, B^* = 1.54, X_0^* = 0.08$, see symbols in Fig. 6c. The most striking difference between order-1 and order-0 bifurcations comes from the asymmetry parameter A. For the order-1 bifurcation, $|A|$ rises up to 2.73, while it is 0.12 for the order-0 bifurcation, i.e. one order of magnitude smaller, consistent with $A \simeq 0$ obtained by Pries et al.[12] for symmetric bifurcations.

In the next Section, we examine the impact of the above correction at order-1 bifurcations on the RBC distribution at network-scale.

2.5 Impact at network-scale

We now check whether correcting the phase separation description at order-1 bifurcations only, i.e. $A = A^{**}$, $B = B^{**}$, $X_0 = X_0^{**}$ at these bifurcations, is sufficient to numerically recover the experimental RBC distribution at network-scale. Fig. 7 shows a comparison between the experimental hematocrit and the tube hematocrit predicted by the corrected network model. Because RBCs are strongly biased toward the daughter branch of the previous bifurcations located on their apex sides (branches α in Fig. 6a, which both feed the network center), this single modification strongly redirects RBCs toward the center of the network (compare Fig. 7b to Fig. 2c), in much closer agreement with the experimental results (Fig. 7a). We quantify this through the correlation between the predicted and measured hematocrit. The Pearson's correlation coefficient increases from $r < 0.8$ to $r = 0.98$, with a slope m much closer to unity ($m = 0.75$), as shown in Fig. 7c, despite the strong simplifications underlying the semi-empirical model (Eqs. 1 and 2) used to correct the description of phase separation at order-1 bifurcations.

We also see that the correction of the phase separation effect accentuates the RBC preferential location in the center of the network, already favored by the baseline flow distribution (see Fig. 2b). This results in a better correlation between high velocity and high hematocrit channels, thus strengthening the tissue Fåhraeus effect (see Supplementary Information SIB and Fig. SI2).

Further correcting the phase separation description in higher order bifurcations (order 2 and 3) slightly improves the prediction accuracy, with an error e $= \frac{\sum_k |H^k_{t,\mathrm{sim}} - H^k_{t,\mathrm{exp}}|}{NH^i_t}$ monotonically decreasing with the number of corrected bifurcations orders (Fig. 8b, blue line). Without correction, we have $e \sim 0.65$. Accounting for upstream asymmetries at order-1 bifurcations significantly reduces the value of e, which is divided by a factor 2. Adding new corrections for higher order bifurcation has much less impact on e, consistent with the results of the sensitivity analysis (Section 2.3).

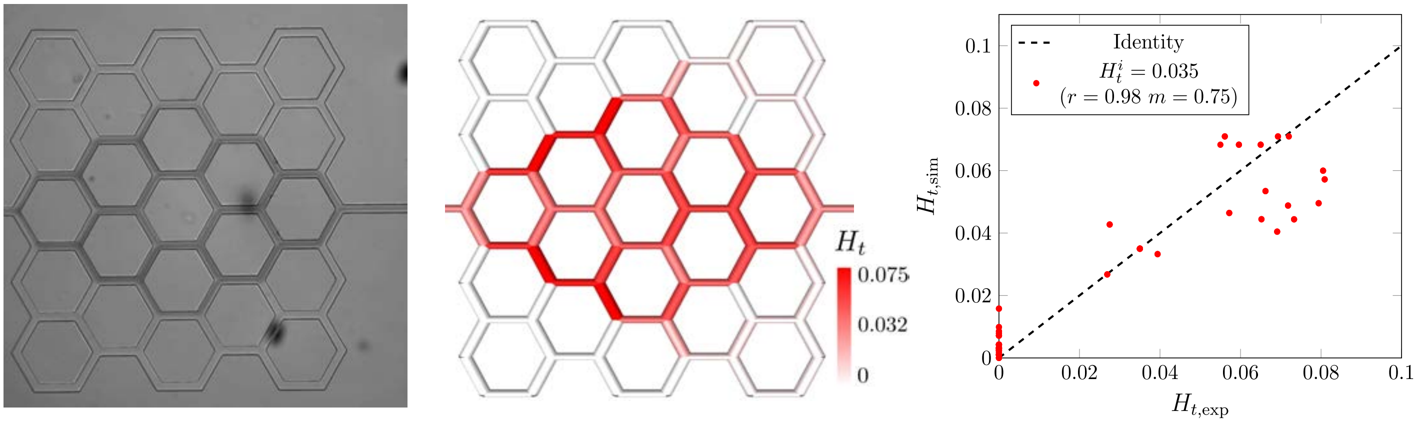

(a) (b) (c)

Figure 7 Correcting phase separation in the order-1 bifurcations is sufficient to restore the RBC pattern observed experimentally in the hexagonal network with $10\mu m$-side channels. (a): Time-averaged intensity field (over 3s). (b) *In silico* predictions of stationary tube hematocrit with phase separation corrected at order-1 bifurcations ($A^{**} = 2.73, B^{**} = 2.78, X_0^{**} = 0.15$). (c) segment by segment comparison between simulated tube hematocrit after phase separation has been corrected at the order-1 bifurcations only, using the effective viscosity previously derived from *in vitro* experiments (Eqs. 9 to 11), and measured tube hematocrit. In the legend, r is the coefficient of correlation and m is the slope of the best linear fit.

Thus, for the small hematocrits considered here, phase separation is strongly affected by upstream bifurcation, as previously identified in[12,16,18]. Moreover, the distribution of RBCs at network-scale is mainly controlled by topological positions of bifurcations within the network. For this hexagonal geometry, this leads to an accentuation of the preferential location of RBCs in the network center, precluding the emergence of a different large scale RBC organization.

Consistently, we expect that reducing the channel cross-sections to $5 \times 5\mu m^2$, where local asymmetries of the RBC profile are hardly possible (see Fig.1b) will only reduce the overall heterogeneity, while still favoring the network center. This is confirmed by the equivalent fluid model (see Supplementary Information SIC and Fig. SI3). Besides, our experiments show that increasing the inlet hematocrit in the wider channels also dampens these local asymmetries, as illustrated in Fig. 8a. This brings the experimental network-scale RBC distributions closer to the initial model predictions, i.e even without correcting phase separation for upstream asymmetries at any bifurcation (see Fig. 8b, where the error monotonically decreases when increasing the inlet hematocrit, whatever the bifurcation order up to which phase separation has been corrected). Overall, we show that, for hexagonal networks, RBCs always favor the network center.

In the next Section, we turn to square networks. We will not reproduce the full analysis as above, but rather show that the same physical ingredients are sufficient to explain the emergence of the two strikingly different patterns described in the Introduction.

3 Application to square networks

For square networks, all vertices except the side vertices are connected to four channels. There exists no quantitative equivalent fluid description of the phase separation at four-connected channel intersections, so that a precise sensitivity analysis as done previously is not possible. Our approach here consists in introducing an approximation of such a separation, but, as a result, the numerical predictions obtained in square networks are only qualitative. However such a qualitative approach is sufficient, as RBC relaxation in square networks has a major impact on the network-scale RBC distribution, by contrast to hexagonal network where we have seen it only leads to small quantitative changes.

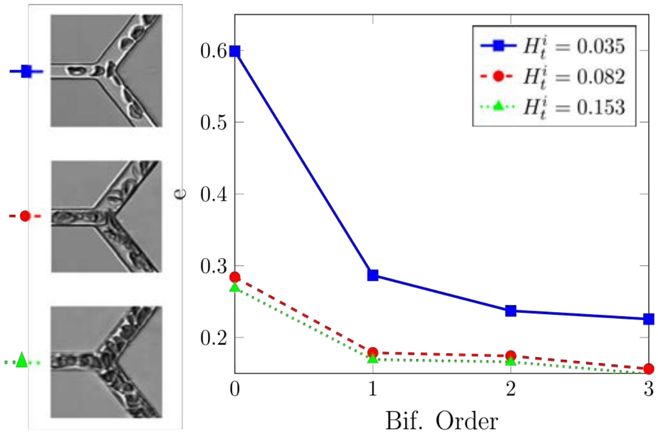

(a) (b)

Figure 8 Order-one bifurcations drive the distribution of red blood cells at network-scale in hexagonal networks with channels of $10 \times 10\mu m^2$ cross-section. (a) Instantaneous snapshots of RBC organization in the order-0 bifurcation of the hexagonal network with $10\mu m$-side channels, showing that increasing the hematocrit reduces the RBC asymmetry in the downstream branches. (b) Average error defined as $e = \frac{\sum_k |H^k_{t,\text{sim}} - H^k_{t,\text{exp}}|}{N H_t^i}$ as a function of the bifurcation order up to which the phase separation is corrected, for different network inlet tube hematocrits H_t^i.

In square networks, we indeed observe a sudden transition between two different patterns of RBC distribution when increasing the confinement, as illustrated in Fig. 1. For conditions similar to the hexagonal case, with channels ($w = 10\mu m$) and dilute RBC suspensions, the RBCs flow preferentially in the central region of the network (Fig. 1a), consistent with the results obtained in hexagonal networks. Upon increasing the confinement, with channels ($w = 5\mu m$), RBCs accumulate in the network corners opposite to the inlet and outlet (Fig. 1b), in agreement with previous theoretical results[24].

To understand this transition, let us first consider the baseline flow, the structure of which does not depend on the confinement. A first property of this flow field is that it favors the central region of the network. The flow divides approximately by a factor two at each successive bifurcation along the network periphery, so that it is of order $1/2^n$ in peripheral channels of order n (i.e. with topological distance n to the inlet segment). By contrast, flows in channels intersecting the i/o axis result from successive divisions and recombinations, and thus the flow decreases much less when progressing towards the network center. As a result, the flow rate in channels intersecting the isopressure line $P = 1/2$ (i.e. channels of order $N-1$) monotonically increases from Q_{min}^{N-1} in the network corners to Q_{max}^{N-1} in the network center. In a 4×4 network, Q_{min}^{N-1}=1/7 and $Q_{max}^{N-1} = 3/14$, as illustrated in Fig. 9a, and the ratio $Q_{max}^{N-1}/Q_{min}^{N-1}$ increases with network size (inset of Fig. 9b).

A second, more subtle, property of the flow field results from the shape of isopressure lines ($P > 1/2$), whose concavity is oriented toward the network inlet (see Supplementary Information SID). In all bifurcations located along the network periphery except at bifurcations of order 0 and $N-2$ where the flow must be balanced, this results in an increase of the flow in the peripheral daughter branch, compared to the flow in the perpendicular daughter branch. The latter lying on the same side than the previous bifurcation apex, we have this time: $Q_\beta > Q_\alpha$ using the same conventions as previously (see Fig. 9a).At bifurcations of order-1, the peripheral channel may receive up to 50% more flow than the other one depending on the network size (Fig. 9b).

Since local flux partitioning favors the peripheral branch at the second bifurcation in the absence of local RBC profile asymmetries, RBCs accumulate in the network corners despite the flow being globally favored in the network center. This distribution is predicted by the previous equivalent fluid network model (Section 6.2) for any confinement level, as well as by a discrete RBC network model (Section 6.3) previously used to study the same configuration[24], as displayed in Fig. 10a[†]. Our observations in networks with the smaller channels (Fig. 1b), where the strong confinement forces RBCs to flow along the channel centerlines, is the first experimental confirmation of this behavior.

When the confinement decreases, however, the RBCs favor the central region (Fig. 1b). To check whether this result can be mainly attributed to the local RBC profile asymmetry upstream order-1 bifurcations, we corrected the description of phase separation at these bifurcations in the same way as in Section 2.4. Fig. 10b shows that this is sufficient to considerably hinder the influence of the baseline flow. Upstream RBC asymmetry is sufficiently strong to deviate most of the RBCs to the central region of the network, against the baseline flow partitioning. This further highlights the critical role played by upstream bifurcations on the RBC distribution at large scale in model networks.

4 Summary of main results

The effect of the upstream bifurcation on the partitioning behavior of a given bifurcation has been largely documented[5,12,16–20,35–37]. Here, we demonstrated for the first time the critical role played by a few key upstream bifurcations on the RBC distribution at the scale of a whole network. We further showed that this non-local, or history, effect is strong enough to induce strikingly different RBC organizations depending on the network architecture.

For sufficiently small hematocrits and confinements, the first bifurcation of the network induces asymmetries of the RBC distribution over the cross-section of its daughter branches. If the length of these daughter branches is shorter than the persistence length of these asymmetries, we observed a strong asymmetry of the RBC partitioning at the next bifurcations, as evidenced by the large value of the asymmetry parameter A obtained in $10\mu m$-side channels. For symmetric networks, this may either lead to accentuating the RBC pattern that would be obtained without any local RBC asymmetry, to attenuating that same pattern, or to switching to another RBC pattern depending on the network architecture. In fact, the architecture controls the baseline flow ratio at these order-1 bifurcations. A rough prediction of the outcome of asymmetric partitioning at their level can be obtained by considering, for this baseline flow ratio, the relative positions of the identity line and of two phase separation diagrams: the symmetric diagram obtained for established RBC flow (blue line in Fig. 11) and the asymmetric diagram accounting for the upstream RBC asymmetries (red line in Fig. 11).

If the branch located on the same side as the previous bifurcation apex receives the highest flow fraction (i.e. ($FQ_B^\alpha > 0.5$) as in hexagonal networks or domain III in Fig. 11), the asymmetric diagram corresponding to this branch (red line) lies above the symmetric diagram (blue line), which lies above the identity line. Thus, the RBC fraction in this branch is even larger than expected in case of symmetric partitioning, which increases the RBC inhomogeneous distribution at network-scale. This scenario would thus also be obtained for a square network if the inlet and outlet were located at the center of opposite sides, as in the hexagonal network (see Supplementary Information SID).

If this branch receives the lowest flow fraction, two domains can be identified in Fig. 11. Either the two phase separation diagrams lie on opposite sides of the identity line (domain II) or not (domain I). In domain II, when the flow fraction is higher than a critical flow ratio ($FQ_c < FQ_B^\alpha < 0.5$), upstream asymmetries lead to reverse partitioning, so that the branch with the lowest flow fraction now collects the highest proportion of RBCs. This directs the RBCs toward flow pathways that would not have been explored without upstream asymmetries, consistent with the results obtained in the the square network with $10 \times 10\mu m^2$ channels. By contrast, in domain I ($0 < FQ_B^\alpha < FQ_c$), the branch collecting the lowest fraction of RBCs is less depleted than expected, which

---

[†] These models provide qualitative results only. For square networks, all vertices except the side vertices are indeed connected to four channels, so that, on one hand, no quantitative equivalent fluid description of the RBC distribution at channel intersections is available. On the other hand, as underlined previously in[17,24], the discrete model is only valid for the highly confined situation ($w = 5\mu m$), where it is reasonable to assume that all RBCs contribute the same singular pressure drop and that they enter the channel with the highest local pressure drop at channel intersections.

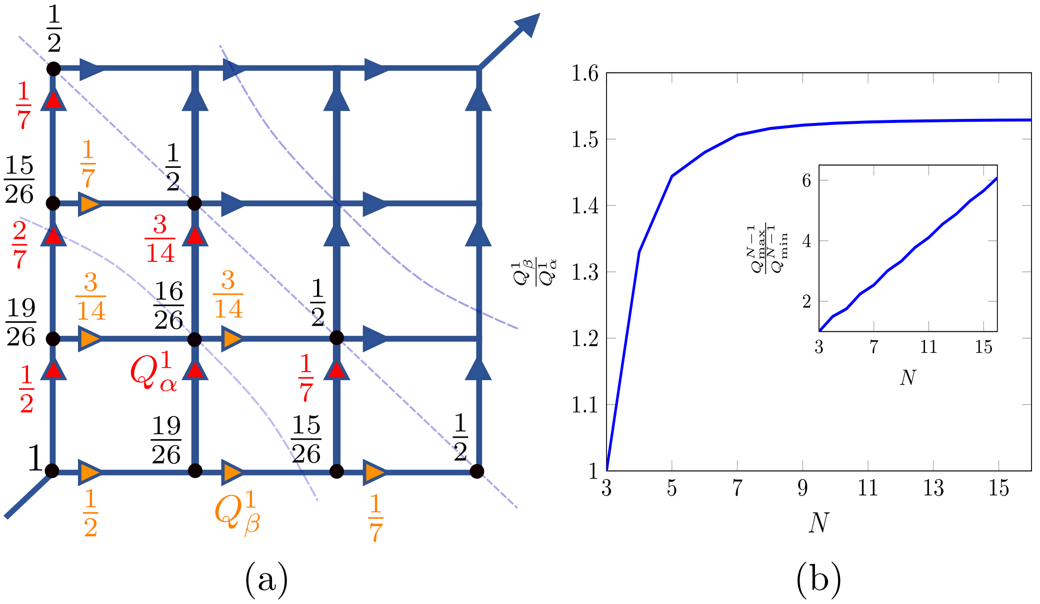

Figure 9 Baseline non-dimensional pressure and flow distribution in a NxN square network ($N = 4$). (a) Black dots: pressures at intersections; red arrows: flow rates in vertical channels; orange arrows: flow rates in horizontal channels. The values in the upper-right hand side of the network can be deduced by symmetry arguments. Dashed lines: from left to right, isopressures $P = 16/26$, $P = 1/2$ and $P = 10/26$. α denotes the branch on the same side than the previous bifurcation apex, so that β is on the network periphery. (b) Flow ratio $\frac{Q^1_\beta}{Q^1_\alpha}$ at order-1 bifurcations as a function of network size N; Inset: Flow ratio $\frac{Q^{N-1}_{max}}{Q^{N-1}_{min}}$ in channels of order $N-1$ as a function of network size N.

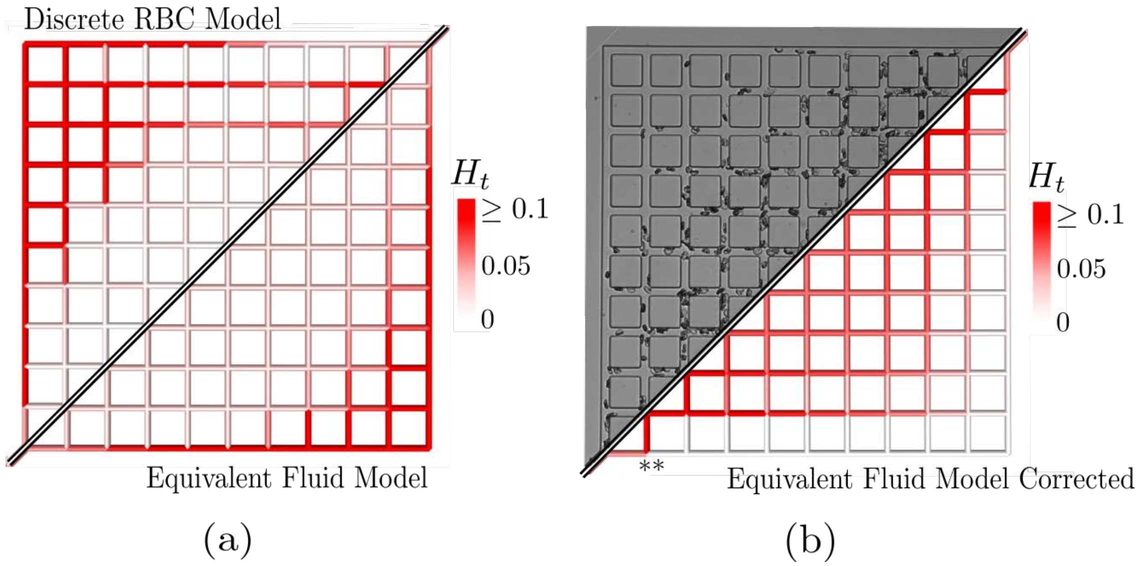

Figure 10 Correcting phase separation in the order-1 bifurcations is sufficient to restore the RBC pattern observed experimentally in the square network with $10\mu m$-side channels. The flow is from the bottom left corner to the top right corner and $H_t^i = 0.05$. (a) *In silico* predictions of stationary tube hematocrit with the discrete red blood cell model presented in Section 6.3 (left anti-diagonal, $\beta = 20$) and the equivalent fluid model presented in Section 6.2 (right anti-diagonal). (b) Experimental (top half) and *in silico* (bottom half) red blood cell distributions. The simulation is performed using the equivalent fluid model with phase separation corrected at the order-1 (**) bifurcations ($A = 15$, $B = 0$, $X_0 = 0$).

reduces the RBC heterogeneity throughout the network. This corresponds to our qualitative observations in square networks with $5 \times 5 \mu m^2$ channels, where the central part of the network (blue area in Fig. 1b) is less depleted compared to the corners (red area) than expected from simulations (Fig. 10a). As already noted, this is counterintuitive as the baseline flow ratio does not depend on the confinement. However, increasing the confinement reduces the asymmetry of the RBC profiles, thus displacing the asymmetric phase separation diagram (red) to the right. This increases the critical flow ratio FQ_c controlling the transition between domains I and II, and reduces the extent of domain II.

These principles reconciliate the contradictory results previously found in the literature about the large scale distribution of RBCs in simple model networks[19,24] by providing a simple phys-

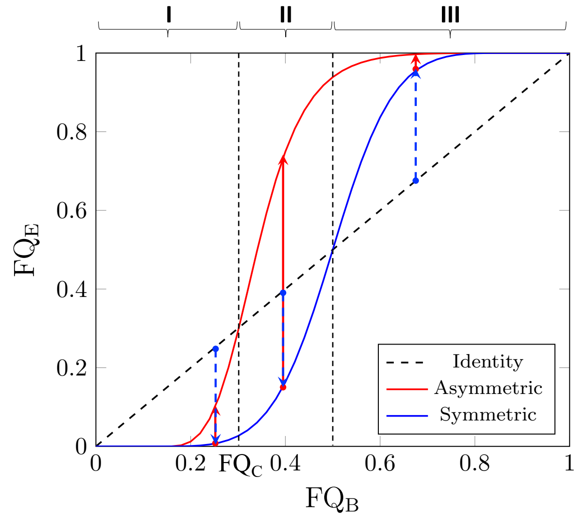

Figure 11 Large scale RBC organization in symmetric networks can be predicted based on the phase separation diagrams at order-1 bifurcations, without (blue) or with (red) upstream asymmetries of the RBC profile. FQ_C is the flow fraction leading to an equal partitioning of RBCs and suspending fluid in the asymmetric case. Domain I : $0 < FQ_B^\alpha < FQ_C$; Domain II: $FQ_C < FQ_B^\alpha < 0.5$; Domain III: $0.5 < FQ_B^\alpha < 1$. See text for more detail.

ical interpretation.

5 Discussion and outlook

The equivalent fluid model needs to be improved in order to describe RBC transport in complex network including asymmetric topologies, distributions of channels width and length and/or multiple inlets/outlets. From our point of view, such a model should consider the transport of an asymmetry parameter describing the relaxation process of the RBC profile within a channel toward its symmetrical established shape. This parameter could then be used to simply correct the phase separation diagram for all bifurcations, whatever their hierarchical position within the network, using the simple semi-empirical model introduced in Section 2.4. For that purpose, a detailed experimental study of RBC lateral migration, in the same spirit as[38], but dealing with higher hematocrits to enable interactions between RBCs, is needed. The main parameters to consider would be the hematocrit, the confinement ratio, and the mean velocity (or alternately the wall shear). According to our experimental results, we anticipate that, for a given mean velocity, increasing the hematocrit or the confinement will decrease the RBC profile relaxation length, so that the scalings in[38] likely provide upper bounds. Alternately, a hybrid approach combining the present equivalent fluid model and highly resolved Direct Numerical Simulations[16,31,39] or reduced order models of RBC collective dynamics[40–42], could be performed at a small number of relevant bifurcations, as identified by the sensitivity analysis approach described in Section 2.3.

These results may help in designing novel microfluidic separation devices and in understanding microvascular physiology or pathology. One central question *in vivo* is whether the main physical ingredient underlined here, that is, the relaxation length of RBCs being longer than the vessel length, is still relevant in microvascular networks. Deep in the capillary bed, the confinement ratio (RBC size over vessel diameter) is typically larger than the highest confinement ratio studied here, so that asymmetries of RBC flow are hardly possible. In the larger arterioles and venules, the hematocrit is much higher than in the present study and closer to the systemic hematocrit ($\simeq$0.4). In these vessels, long-lasting asymmetries of the RBC profile are also unlikely. However, the situation is different for vessels lying in between, i.e. small arterioles, precapillary arterioles, and, possibly, large capillaries. These lie in a range of diameters and hematocrits, which, in principle, make such asymmetries possible. Their diameter range in the mouse brain is typically between 6 and 17 micrometers (see, e.g.[43]), which, considering a mice to human RBC volume ratio of 0.86[44], corresponds to the confinement encountered in channels of widths between 7 and $20\mu m$. Furthermore, their hematocrit is typically between 0.02 and 0.2[45].

Corrugations of the vessel walls by protruding endothelial cells or the presence of the glycocalyx, a polysaccharid brush that contributes to reducing the effective diameter of vessels[46–48], may further shorten the relaxation length *in vivo*. Even if this is the case, their median length to diameter ratio is typically smaller than ten[49], i.e. the *in vivo* threshold value above which the previous bifurcation has no influence on the next one[12].

Interestingly, these vessels are also covered by a variety of contractile cell types, including smooth muscle cells, ensheathing pericytes and mesh pericytes[43], which participate to blood flow regulation within the brain as a function of neuronal activity (neurovascular coupling)[50]. Therefore, it is theoretically possible that the above phenomena participate to redirect the RBC flux from inactive brain regions to active brain regions, or from arterio-venular anastomoses to active brain regions, by locally modulating vessel diameters so that the fractional flow reaches a critical value.

Moreover, several pathologies may involve abnormal, highly heterogeneous, vascular architectures with a larger occurrence of short vessel segments and/or may contribute to increase the RBC relaxation length. In tumors, for example, the vessel length to diameter ratio is notably decreased, which has been suggested to affect hematocrit distribution in tumor vascular networks and drive heterogeneous oxygenation of tumor tissue[5]. Damage to the glycocalyx, e.g. resulting from diabetes, inflammation or hypoxia, has been shown to reduce the thickness of the cell free layer[51], and is thus likely to increase the RBC relaxation length. Consistent with our results, pharmacological degradation of the glycocalyx in the hamster led to increased microvascular hematocrit heterogenity, with both a drastic decrease ($\sim$ 35%) of the number of capillaries perfused by RBCs and a drastic increase ($\sim$ 70%) of the mean hematocrit in these capillaries, while vessel diameters and blood velocity remained statistically unchanged[48]. This has been interpreted as resulting from increased platelet or leucocyte adhesion to the vessel walls induced by the glycocalyx degradation[52], but our results suggest that increased RBC relaxation length may also play a role. Thus, the above results may help understand the development of microvascular dysfunction in a large range of diseases.

6 Materials and Methods

6.1 Experiments

6.1.1 Network fabrication

Networks with either hexagonal (Fig. 2) or square (Fig. 1) patterns, made of microchannels of square cross-sections, are fabricated by soft photolithography as described in Roman et al.[14,53] with the following modifications: the PDMS cast is sealed with a $100\mu m$ thick microscope glass coverslip by applying manual pressure to remove trapped air and then pouring liquid PDMS on its edges. All channels in the network, including the inlet and outlet channels, have identical dimensions, *i.e.* $5\text{x}5\mu m^2$ or $10\text{x}10\mu m^2$ for the cross-section and $50\mu m$ for the length, except $15mm$ long rectangular distribution and drainage channels placed upstream and downstream. Before use, networks are incubated overnight with a solution of Phosphate Buffered Saline (PBS) containing 2.5mg/ml Bovine Serum Albumine (BSA, Eurobio) in order to prevent RBC adhesion to microchannel walls.

6.1.2 Red blood cell suspensions

Fresh whole blood samples from healthy volunteers are provided by the Etablissement Français du Sang (EFS) in EDTA tubes for anticoagulation. These samples are then centrifugated and the RBC pellet is collected and washed three times using PBS. To prevent sedimentation during the experiments, red blood cells are resuspended in an appropriate isodense solution following[14,34], enabling to control the feed hematocrit. All suspensions are stored at +4°C and used within 48 hours after collection.

6.1.3 Red blood cell flow and imaging

The flow is generated by imposing a pressure drop between the microfluidic network inlet and outlet in the range of 30 to 90 mbar using a pressure controller (MicroFluidics Control System 8C, Fluigent), ensuring very short response times when the set pressure drop is changed and good stability over long periods. The network is then placed on the stage of a Leica DMRXA2 microscope, glass cover slip facing a $\times 20$ ($NA = 0.4$) long-working distance objective. We record image sequences of the flow using an external collimated light source (Leica EL6000) and a fast camera (pco.dimax S). Typical image sequences are composed of $\sim$6000 snapshots, such as the one shown in Figs. 1 and 2a, corresponding to a physical time of $\sim$3 s. These image sequences are used to deduce hematocrit profiles, tube hematocrits and RBC velocities, as summarized in Sections 6.1.4 and 6.1.5. Noteworthy, the total duration of the sequences is longer than the 0.7 s used by[16] for averaging temporal data and ensures that all time-averaged quantities considered in the present paper are converged.

6.1.4 Hematocrit profiles and tube hematocrit

For a given position (z) along the microchannel axis, the hematocrit profile $H(x)$ is defined as the time-averaged volume fraction occupied by RBCs in the whole channel depth, *i.e.* integrated over y. To determine the hematocrit profile, we first sub-sample the image sequences, keeping one of ten snapshots, to avoid considering the same RBC multiple times at the same location. We then compute the optical density profile $\mathrm{OD}(x)$ from the time-averaged greyscale intensity profile $I(x)$ as follows[13,14,19,54,55]:

$$\mathrm{OD}(x) = -\log_{10}\left(\frac{I(x)}{I_{0(x)}}\right), \tag{3}$$

where $I_0(x)$ is a reference intensity profile. Following Sherwood et al.[13], we assumed here that $I_0(x)$ is constant and equal to the greyscale value in the PDMS far from any channel. This is a reasonable approximation except in the close vicinity of channel walls (Fig. SI5A), where we infer the optical density profile by linear extrapolation[13], as summarized in Supplementary Information SIE and Fig. SI5B-E.

To relate the local tube hematocrit value $H(x)$ to the optical density, we used Leja slides (Leja Products B.V.). These are manufactured Hele-Shaw cells with finely controlled depths (10 or $20\mu m$) and much larger length and width ($\sim 2cm$). We filled each slide extremely slowly with a small volume of RBC suspension of known feed hematocrit, so as to reduce as much as possible local hematocrit heterogeneities within the slide, while ensuring it contained the whole injected volume. In that way, the local hematocrit is everywhere equal to the feed hematocrit, which enables precise calibration of the optical density, even for suspensions where RBCs are not individually discernible (for more details see Supplementary Information SIE and Fig. SI6.

Finally, we derive the tube hematocrit H_t associated with each microchannel by averaging $H(x)$ over the channel width W at the output of the channel ($z_{\mathrm{output}} = 45\mu\mathrm{m}$):

$$H_t = \left[\frac{1}{W}\int_{-W/2}^{W/2} H(x)dx\right]_{z=45\mu\mathrm{m}}. \tag{4}$$

6.1.5 Red blood cell velocities

For the channel size and hematocrit range considered in this study, we expect flat velocity profiles to be obtained in regions where the flow is established, *i.e.* sufficiently far from each channel input and output. Thus, we define the RBC velocity associated with a given microchannel as the time-averaged velocity measured at mid-channel length ($z = 25\mu\mathrm{m}$). The latter is deduced from the image sequences using either particle tracking velocimetry (*i.e.* measuring the time required by RBCs to travel a prescribed distance of $10\mu m$ from mid-channel) or particle image velocimetry (PIV), using the method of sum of correlation[56] implemented in DaVis (LaVision) with RBCs as tracers[57]. PIV further enables to estimate the (depth-averaged) velocity profile across a given channel, in areas where the flow structure is more complex, i.e. at the level of bifurcations.

6.2 Modeling and simulations: equivalent fluid model

While it is possible to simulate RBC suspension flows in networks by describing each RBC individually[16,31,39], it remains computationally challenging, especially if a large range of flow conditions and geometries is to be considered. Thus, following[2,44,58–60], we describe RBCs suspensions as single-phase, non-Newtonian fluids, with 1/ tube hematocrits (volume fractions) $H_t = \frac{\mathcal{V}_{\mathrm{RBC}}}{\mathcal{V}}$ representing the RBCs, 2/ effective viscosities representing the time-averaged viscous dissipation associated with interactions among RBCs and with the suspending fluid and the vessel walls (Fåhraeus-Lindqvist effect), and 3/ bifurcation laws representing, on average, the unequal distribution of RBCs at diverging bifurcations (phase separation effect)[61]. Altogether, these assumptions make it possible to simplify the description of hexagonal and square networks by considering them as graphs, *i.e.*, as the union between a set of vertices $\{i\}$, corresponding to the network inlet and outlet and all its bifurcations, and a set of edges, defined as pair of vertices $\{(i,j)\}$, corresponding to the microchannels. In this representation, determining the pressure P_i at every vertex, the total flow rate Q_{ij} and discharge hematocrit (flow rate fraction) $H_{d,ij} = \frac{Q_{\mathrm{RBC},ij}}{Q_{ij}}$ in every edge is sufficient to fully describe the flow withing the network.

The tube hematocrit is then deduced from the discharge hematocrit taking the Fåhraeus effect[62] into account, as follows

$$\frac{H_{t,ij}}{H_{d,ij}} = H_{d,ij} + (1-H_{d,ij})(1+1.7e^{-0.36\zeta_{ij}} - 0.6e^{-0.01\zeta_{ij}}), \tag{5}$$

where ζ is the hydraulic diameter of the microchannel in micrometers. Our previous experiments have indeed shown that this expression, adapted from the empirical description derived from *in vitro* experiments performed with rat RBCs in cylindrical glass tubes[2,44], is well suited to evaluate the Fåhraeus effect in the flow regimes considered here[14].

6.2.1 Hexagonal networks

In order to solve the blood flow problem in the hexagonal networks presented in Fig. 2, we start by writing the balances of blood flow rates

$$\sum_j Q_{ij} = 0, \tag{6}$$

and RBC flow rates

$$\sum_j H_{d,ij} Q_{ij} = 0, \tag{7}$$

at each vertex i of the network, excluding the boundary vertices. We then write the momentum balance between the inlet and outlet of each channel

$$Q_{ij} = \frac{\pi d_{\mathrm{h},ij}^4}{128\mu_{\mathrm{eff},ij} L_{ij}} \left(P_i - P_j\right), \tag{8}$$

where L_{ij} represents the channel length, $d_{\mathrm{h},ij}$ its hydraulic diameter (in SI units). The above equation is similar to Poiseuille's equation, except that the fluid viscosity has been replaced by $\mu_{\mathrm{eff},ij}$, i.e. the effective viscosity of the fluid within the channel. Due to the RBC presence, its velocity profile is blunted at the center of the channel[11,18,63] with a slip velocity at wall[18,34,64]. The associated viscous dissipation has been measured by[65], who performed *in vitro* experiments using human RBCs in plasma. This yielded the following empirical description for the Fåhraeus-Lindqvist effect

$$\mu_{\mathrm{eff},ij} = \mu_p \left(1 + (\mu_{0.45,ij} - 1)\, \frac{\left(1-H_{d,ij}\right)^{C_{ij}} - 1}{(1-0.45)^{C_{ij}} - 1}\right), \tag{9}$$

where $\mu_p \approx 10^{-3}$Pa.s represents the viscosity of plasma and where

$$\mu_{0.45,ij} = 220e^{-1.3\zeta_{ij}} + 3.2 - 2.44e^{-0.06\zeta_{ij}^{0.645}}, \tag{10}$$

$$C_{ij} = \frac{0.1 - \left(0.1\zeta_{ij}\right)^{12}\left(0.8 + e^{-0.075\zeta_{ij}}\right)}{0.1 + \left(0.1\zeta_{ij}\right)^{12}}, \tag{11}$$

are two functions of the vessel diameter expressed in micrometers ($\zeta_{ij} = 10^6 d_{\mathrm{h},ij}$).

Altogether, Eqs. 6 to 11 form a linear system, which is straightforward to solve if the distribution of discharge hematocrits is known. However, RBC and plasma are distributed non-proportionally between the daughter channels of diverging bifurcations (i.e. vertices with one entry channel and two daughter channels, such as $*$ and $**$ in Fig.4a)[12,66]. This phase separation effect must be accounted for to determine the discharge hematocrits within the network. For that purpose, we write the following phase separation model

$$H_{d,\alpha} = \frac{\mathrm{FQ}_E^\alpha}{\mathrm{FQ}_B^\alpha} H_{d,e}, \tag{12}$$

$$H_{d,\beta} = \frac{1-\mathrm{FQ}_E^\alpha}{1-\mathrm{FQ}_B^\alpha} H_{d,e}, \tag{13}$$

where $e = \{i,j\}$ denotes the entry channel, $\alpha = \{i,k\}$ and $\beta = \{i,l\}$ denote the daughter channels and where $\mathrm{FQ}_E^\alpha = \frac{Q_{RBC,\alpha}}{Q_{RBC,e}}$ and $\mathrm{FQ}_B^\alpha = \left|\frac{Q_\alpha}{Q_e}\right|$ represent the fraction of RBC flow rate and total flow rate going from the entry channel to the daughter channel α. This fractional blood flow is described using the following empirical description, based on in vivo experiments performed in rats[12,28] and later adapted to human blood[44]

$$\mathrm{FQ}_E^\alpha = \begin{cases} 0 \quad \text{when } \mathrm{FQ}_B^\alpha < X_0 \\[2ex] \dfrac{\exp\left(A + B\mathrm{logit}\left(\frac{\mathrm{FQ}_B^\alpha - X_0}{1-2X_0}\right)\right)}{1+\exp\left(A + B\mathrm{logit}\left(\frac{\mathrm{FQ}_B^\alpha - X_0}{1-2X_0}\right)\right)} \quad \text{when } X_0 < \mathrm{FQ}_B^\alpha < 1 - X_0 \\[2ex] 1 \quad \text{when } \mathrm{FQ}_B^\alpha > 1 - X_0 \end{cases} \tag{14}$$

Here, $\mathrm{logit}(x) = \ln\left(\frac{x}{1-x}\right)$ and

$$A = -15.47 \left(\frac{\zeta_\alpha - \zeta_\beta}{\zeta_\alpha + \zeta_\beta}\right)\left(\frac{1-H_{d,e}}{\zeta_e}\right) \tag{15}$$

encompasses the effects induced by the asymmetries in the bifurcation geometry,

$$B = 1 + 8.13\left(\frac{1-H_{d,e}}{\zeta_e}\right) \tag{16}$$

controls the intensity of the non-linearity and

$$X_0 = 1.12\left(\frac{1-H_{d,e}}{\zeta_e}\right) \tag{17}$$

corresponds to the threshold below which no RBC enters the bifurcation outlet with the smallest blood flow rate. Noteworthy, our previous experiments have shown that these expressions are well suited to describe phase separation in the flow regimes considered here[14]. Altogether, Eqs. 6 to 17 form a non-linear problem that we solve iteratively (see more detail in Supplementary Information SIF.), after having prescribed compatible initial and boundary conditions.

To that end, we impose a constant discharge hematocrit at the network inlet, typically ranging from 0.035 to 0.155, which corresponds to the experimental values, and consider the network to be initially filled with suspending fluid ($H_{d,ij} = 0$). We also prescribe a constant pressure drop ΔP between the network inlet and outlet. We point out that, for shear rates (estimated by V_{RBC}/W) typically above $50s^{-1}$, the apparent viscosities do neither depend on the shear rate[61,67] nor, as a result, on the pressure drop, so that blood flow rates in individual channels linearly depend on the channel pressure drop (Eq. 8). In addition, discharge hematocrits only depends on the ratio of blood flow rates (Eqs. 12 to 14). Thus, the solution of the blood flow problem depends linearly on ΔP and the flow rates (or velocities) normalized by the flow rate (or velocity) in the inlet channel, as displayed in Fig. 3b, do not depend on ΔP.

6.2.2 Square networks

The square networks presented in Fig. 10 are similar in all aspects to hexagonal networks except that most of their vertices are connected to four neighbours instead of three and that their single inlet and outlet are located in lower-left and upper-right corners, respectively.

This makes it necessary to modify the description of the phase separation effect at diverging bifurcations. For the case of a four-connected diverging bifurcation in a generic square network, there are two possible configurations: 1/two feeding vessels and two daughter vessels, or 2/, one feeding vessel and three daughter vessels. Here, since the network inlet and outlet are located at opposite corners, only the first configuration can occur, due to the topology of the baseline flow problem at hand (similar to Fig. 9a) and because we focus on low discharge hematocrits regimes for which RBC have a small effect on the effective viscosity. In this case, we consider the two entry vessels $\{i,j\}$ and $\{i,k\}$ as a single equivalent entry vessel, with the following diameter, blood flow rate and discharge hematocrit

$$d_{\mathrm{e}} = \sqrt{d^2_{\mathrm{h},ij} + d^2_{\mathrm{h},ik}}, \tag{18}$$

$$Q_{\mathrm{e}} = |Q_{ij}| + |Q_{ik}|, \tag{19}$$

$$H_{d,\mathrm{e}} = \left(H_{d,ij}|Q_{ij}| + H_{d,ik}|Q_{ik}|\right)/Q_{\mathrm{e}}. \tag{20}$$

We then solve equations 12 to 17 using these effective quantities, and deduce the discharge hematocrit in daughter vessels α and β.

6.2.3 Sensitivity analysis

The equivalent fluid model described above makes fast computations of the RBC distribution at network-scale possible. Thus, it makes it possible to evaluate the influence of the phase separation effect occurring at each diverging bifurcation on the discharge hematocrit of each vessel by computing the total Sobol indices[68]. For that purpose, we first arbitrarily label α one of the daughter branches of each bifurcation. We then rewrite equation 12 and 13 considering, for each divergent bifurcation, FQ_E^{α} as an independent random variable following a uniform distribution between 0 and 1. We then use the JansenSensitivityAlgorithm embedded in the Python library OpenTurns[69] to sample the combined random distributions $\sim 10^6$ times and to solve for the associated blood flow problems (Eqs. 6 to 13) in the network.

6.3 Modeling and simulations: discrete red blood cell model

In this section, we present the model used in Fig. 10a. This model can be seen as an alternative to the continuous blood flow model presented in section 6.2.1, that still relies on a network approach while treating the RBCs as discrete particles. Initially developped by Schmid-Schönbein et al.[17] and later improved by Obrist et al.[24] and Schmid at al.[25], this model tracks individual RBCs throughout networks of very narrow microchannels ($\zeta \simeq 5$microns) assuming single file flow. The velocity of each RBC in a given channel $\{i,j\}$ is supposed to be constant so that

$$V_{\mathrm{RBC},ij} = \theta_{ij} V_{ij}, \tag{21}$$

where $V_{\mathrm{RBC},ij}$ represents the RBC velocities, V_{ij} is the blood average velocity and $1 \leq \theta_{ij} \leq 2$ is a parameter which is taken equal to one by Obrist et al.[24] but is defined here as

$$\theta_{ij} = \frac{H_{t,ij}}{H_{d,ij}}, \tag{22}$$

in order to explicitly take the Fåhraeus effect into account, as parametrized by equation 5. The blood velocity in each vessel is deduced using Eq. 8, with an additional resistance to flow proportional to the number of RBCs in each channel, yielding

$$\mu_{\mathrm{eff},ij} = \mu_p \left(1 + \beta_{ij} H_{t,ij}\right), \tag{23}$$

where β_{ij} represents an apparent intrinsic viscosity of individual RBCs, and is left as a free parameter to explore the effect of flow-RBC interactions on the distribution of RBCs. For the phase separation at bifurcations, following Obrist et al.[24], we assume that RBCs always favor the daughter vessel with the highest flow rate, i.e. corresponding to the asymptotic behavior of phase separation (Eqs. 14 to 17) in very narrow channels[61].

Conflicts of interest

There are no conflicts of interest to declare.

Acknowledgments

We gratefully acknowledge S. Cazin, M. Ogier and D. Bourrier for technical support, Fédération FERMAT, GDR Mécabio and the anonymous reviewers for their constructive suggestions. The research leading to these results has received funding from the European Research Council under the European Union's Seventh Framework Program (FP7/2007-2013) Consolidator Brainmicroflow, ERC grant agreement n^o 615102 and from the NIH (awards R21CA214299 and 1RF1NS110054). It was performed using HPC resources from CALMIP (Grant 2016-P1541) and the LAAS-CNRS technological platform from the french RENATECH network (P-14-01199). YD was funded by the H2020 program Starting Bebop, ERC grant agreement n^{o} 803074.

References

1 S. P. Sutera and R. Skalak, Annual Review of Fluid Mechanics, 1993, **25**, 1–20.

2 A. R. Pries, T. W. Secomb, P. Gaehtgens and J. F. Gross, Circulation Research, 1990, **67**, 826–834.

3 M. Desjardins, R. Berti, J. Lefebvre, S. Dubeau and F. Lesage, Neurobiology of Aging, 2014, **35**, 1947–1955.

4 A. Villringer, A. Them, U. Lindauer, K. Einhäupl and U. Dirnagl, Circulation Research, 1994, **75**, 55–62.

5 M. O. Bernabeu, J. Köry, J. A. Grogan, B. Markelc, A. Beardo, M. dÁvezac, R. Enjalbert, J. Kaeppler, N. Daly, J. Hetherington, T. Krüger, P. K. Maini, J. M. Pitt-Francis, R. J. Muschel, T. Alarcón and H. M. Byrne, Proceedings of the National Academy of Sciences, 2019, 27811–27819.

6 J. C. Cruz-Hernández, O. Bracko, C. J. Kersbergen, V. Muse, M. Haft-Javaherian, M. Berg, L. Park, L. K. Vinarcsik, I. Ivasyk, Y. Kang, M. Cortes-Canteli, M. Peyrounette, V. Doyeux, A. Smith, J. Zhou, G. Otte, J. D. Beverly, E. Davenport, Y. Davit, S. Strickland, C. Iadecola, S. Lorthois, N. Nishimura and C. B. Schaffer, Nature Neuroscience, 2019, 413–420.

7 F. Goirand, T. Le Borgne and S. Lorthois, Nature Communications, in revision.

8 Y. C. Fung, Biodynamics: Circulation, Springer New York, New York, NY, 1984.

9 A. Kumar and M. D. Graham, Soft Matter, 2012, **8**, 10536.

10 T. Secomb, Annual Review of Fluid Mechanics, 2017, **49**, 443–461.

11 A. R. Pries, T. W. Secomb and P. Gaehtgens, Cardiovascular Research, 1996, **32**, 654–667.

12 A. R. Pries, K. Ley, M. Claassen and P. Gaehtgens, Microvascular research, 1989, **38**, 81–101.

13 J. M. Sherwood, E. Kaliviotis, J. Dusting and S. Balabani, Biomechanics and Modeling in Mechanobiology, 2014, **13**, 259–273.

14 S. Roman, A. Merlo, P. Duru, F. Risso and S. Lorthois, Biomicrofluidics, 2016, **10**, 034103.

15 P. M. Rasmussen, T. W. Secomb and A. R. Pries, Microcirculation, 2018, **25**, e12445.

16 P. Balogh and P. Bagchi, Physics of Fluids, 2018, **30**, 051902.

17 G. W. Schmid-Schönbein, R. Skalak, S. Usami and S. Chien, Microvascular Research, 1980, **19**, 18–44.

18 J. M. Sherwood, D. Holmes, E. Kaliviotis and S. Balabani, PLOS ONE, 2014, **9**, 1–13.

19 A. Mantegazza, F. Clavica and D. Obrist, Biomicrofluidics, 2020, **14**, 014101.

20 Q. Zhou, J. Fidalgo, M. O. Bernabeu, M. S. N. Oliveira and T. Krüger, Soft Matter, 2021, 3619–3633.

21 Z. Wang, Y. Sui, A.-V. Salsac, D. Barthes-Biesel and W. Wang, Journal of Fluid Mechanics, 2018, **849**, 136–162.

22 A. R. Pries and P. Gaehtgens, in Dispersion of Blood Cell Flow in Microvascular Networks, ed. J.-S. Lee and T. C. Skalak, Springer New York, New York, NY, 1989, pp. 50–64.

23 A. R. Pries, T. W. Secomb and P. Gaehtgens, American Journal of Physiology-Heart and Circulatory Physiology, 1995, **269**, H1713–H1722.

24 D. Obrist, B. Weber, A. Buck and P. Jenny, Philosophical Transactions of the Royal Society A: Mathematical, Physical and Engineering Sciences, 2010, **368**, 2897–2918.

25 F. Schmid, J. Reichold, B. Weber and P. Jenny, American Journal of Physiology - Heart and Circulatory Physiology, 2015, **308**, H733–H742.

26 P. Blinder, P. S. Tsai, J. P. Kaufhold, P. M. Knutsen, H. Suhl and D. Kleinfeld, Nature Neuroscience, 2013, **16**, 889–897.

27 A. F. Smith, V. Doyeux, M. Berg, M. Peyrounette, M. Haft-Javaherian, A. E. Larue, J. H. Slater, F. Lauwers, P. Blinder, P. Tsai, D. Kleinfeld, C. B. Schaffer, N. Nishimura, Y. Davit and S. Lorthois, Frontiers in Physiology, 2019, **10**, 233.

28 A. R. Pries, B. Reglin and T. W. Secomb, American Journal of Physiology - Heart and Circulatory Physiology, 2003, **284**, H2204–H2212.

29 N. J. Karst, B. D. Storey and J. B. Geddes, Bulletin of Mathematical Biology, 2015, **77**, 1377–1400.

30 N. J. Karst, J. B. Geddes and R. T. Carr, Bulletin of Mathematical Biology, 2017, **79**, 662–681.

31 P. Balogh and P. Bagchi, Biophysical Journal, 2017, **113**, 2815–2826.

32 B. M. Fenton, R. T. Carr and G. R. Cokelet, Microvascular Research, 1985, **29**, 103 – 126.

33 G. Enden and A. S. Popel, ASME Journal of Biomechanical Engineering, 1994, **116**, 79–88.

34 S. Roman, S. Lorthois, P. Duru and F. Risso, Microvascular Research, 2012, **84**, 249–261.

35 R. T. Carr and L. L. Wickham, Microvascular Research, 1990, **40**, 179–190.

36 B. W. Roberts and W. L. Olbricht, AIChE Journal, 2003, **49**, 2842–2849.

37 G. R. Cokelet, Hemorheology and Hemodynamics, Morgan & Claypool Life Sciences, 2011.

38 S. Losserand, G. Coupier and T. Podgorski, Microvascular Research, 2019, **124**, 30–36.

39 C. Iss, D. Midou, A. Moreau, D. Held, A. Charrier, S. Mendez, A. Viallat and E. Helfer, Soft Matter, 2019, **15**, 2971–2980.

40 X. Li, P. M. Vlahovska and G. E. Karniadakis, Soft Matter, 2013, **9**, 28–37.

41 D. A. Fedosov, W. Pan, B. Caswell, G. Gompper and G. E. Karniadakis, Proceedings of the National Academy of Sciences, 2011, **108**, 11772–11777.

42 D. Alexeev, L. Amoudruz, S. Litvinov and P. Koumoutsakos, Computer Physics Communications, 2020, **254**, 107298.

43 R. I. Grant, D. A. Hartmann, R. G. Underly, A.-A. Berthiaume, N. R. Bhat and A. Y. Shih, Journal of Cerebral Blood Flow & Metabolism, 2019, **39**, 411–425.

44 S. Lorthois, F. Cassot and F. Lauwers, NeuroImage, 2011, **54**, 1031–1042.

45 H. H. Lipowsky, S. Usami and S. Chien, Microvascular Research, 1980, **19**, 297–319.

46 A. R. Pries, T. W. Secomb, T. Gessner, M. B. Sperandio, J. F. Gross and P. Gaehtgens, Circulation Research, 1994, **75**, 904–914.

47 A. R. Pries, AJP: Heart and Circulatory Physiology, 2005, **289**, H2657–H2664.

48 P. Cabrales, B. Y. S. Vazquez, A. G. Tsai and M. Intaglietta, Journal of Applied Physiology, 2007, **102**, 2251–2259.

49 S. Lorthois, F. Lauwers and F. Cassot, Microvascular Research, 2014, **91**, 99–109.

50 D. A. Hartmann, A.-A. Berthiaume, R. I. Grant, S. A. Harrill, T. Noonan, J. Costello, T. Tieu, K. McDowell, A. Faino, A. Kelly and A. Y. Shih, Nature Neuroscience, 2021, **24**, 633–645.

51 C. S. Alphonsus and R. N. Rodseth, Anaesthesia, 2014, **69**, 777–784.

52 C. J. Zuurbier, C. Demirci, A. Koeman, H. Vink and C. Ince, Journal of Applied Physiology, 2005, **99**, 1471–1476.

53 S. Roman, S. Lorthois, P. Duru and F. Risso, Journal of Biomechanics, 2012, **45**, S35.

54 H. H. Lipowsky, S. Usami, S. Chien and R. N. Pittman, Microvascular Research, 1982, **24**, 42 – 55.

55 A. R. Pries, G. Kanzow and P. Gaehtgens, American Journal of Physiology-Heart and Circulatory Physiology, 1983, **245**, H167–H177.

56 E. Antoine, C. Buchanan, K. Fezzaa, W.-K. Lee, M. N. Rylander and P. Vlachos, PLOS ONE, 2013, **8**, 1–8.

57 C. Poelma, A. Kloosterman, B. P. Hierck and J. Westerweel, PLOS ONE, 2012, **7**, 1–12.

58 R. Guibert, C. Fonta and F. Plouraboué, Journal of Cerebral Blood Flow & Metabolism, 2010, **30**, 1860–1873.

59 B. C. Fry, J. Lee, N. P. Smith and T. W. Secomb, Microcirculation, 2012, **19**, 530–538.

60 A. A. Linninger, I. G. Gould, T. Marinnan, C. Y. Hsu, M. Chojecki and A. Alaraj, Annals of Biomedical Engineering, 2013, **41**, 2264–2284.

61 S. Lorthois, in Dynamics of blood cell suspensions in micro flow, CRC Press, 2019, ch. Blood suspension in a network.

62 R. Fåhraeus, Physiological Reviews, 1929, **9**, 241–274.

63 T. P. Santisakultarm, N. R. Cornelius, N. Nishimura, A. I. Schafer, R. T. Silver, P. C. Doerschuk, W. L. Olbricht and C. B. Schaffer, AJP: Heart and Circulatory Physiology, 2012, **302**, 1367–1377.

64 M. Berg, Y. Davit, M. Quintard and S. Lorthois, Journal of Fluid Mechanics, 2020, **884**, A39.

65 A. R. Pries, D. Neuhaus and P. Gaehtgens, American Journal of Physiology-Heart and Circulatory Physiology, 1992, **263**, H1770–H1778.

66 Y. C. Fung and B. W. Zweifach, Annual Review of Fluid Mechanics, 1971, **3**, 189–210.

67 W. Reinke, P. Gaehtgens and P. C. Johnson, American Journal of Physiology-Heart and Circulatory Physiology, 1987, **253**, H540–H547.

68 I. M. Sobol, Mathematical modeling and computational experiment, 1993, **1**, 407–414.

69 M. Baudin, A. Dutfoy, B. Iooss and A.-L. Popelin, in OpenTURNS: An Industrial Software for Uncertainty Quantification in Simulation, ed. R. Ghanem, D. Higdon and H. Owhadi, Springer International Publishing, Cham, 2016, pp. 1–38.

Soft Matter

ARTICLE TYPE

Cite this: DOI: 00.0000/xxxxxxxxxx

Supplementary Information for: A few upstream bifurcations drive the spatial distribution of red blood cells in model microfluidic networks

Adlan Merlo,‡ Maxime Berg,‡ Paul Duru, Frédéric Risso, Yohan Davit, and Sylvie Lorthois

SIA. Supplementary results: Multiple equilibria in microvascular networks

The problem formed by Eqs. 6-17 is non-linear and may therefore have several equilibrium solutions. Karst et al. showed, using continuation methods, that for blood flow in 2D Voronoi-like networks, the number of equilibria was an increasing function of the inlet tube hematocrit, although they noted that such equilibria were lying close to each other[1]. However, they used a customized phase separation relationship along with the expression for the effective viscosity of the blood deduced from in vivo experiments. In particular, the latter induces a much stronger feedback of the RBC on the flow compared to the in vitro expression used in this work, and this feedback is a key in the emergence of multiple equilibria.

Given the low inlet tube hematocrit considered ($H_t^i = 0.035$) and the weak feedback of the RBC on the flow (see Fig. 3b), we suspect that the discrepancies between experiments and simulations highlighted in Fig. 3a cannot come from our numerical method converging towards to a wrong solution. Still, we tried, using the numerical method presented in Section SID (Eqs. SI.4 to SI.8) to trigger different equilibrium solutions in the hexagonal network. To do so, we introduced a relaxation factor $0 < \gamma \leq 1$ so that

$$H_{d,ij}^{n+1} = \gamma H_{d,ij}^{s} + (1-\gamma) H_{d,ij}^{n}, \tag{SI.1}$$

where H_d^s represents the solution of the system formed by equations SI.4 and SI.8. This relaxation factor is a free parameter and allows us to control the convergence of the numerical method. We then solved the blood flow problem for an increasing inlet tube hematocrit (from $H_{t,\text{inlet}} = 0$ to $H_{t,\text{inlet}} = 0.9$). For each value of the inlet tube hematocrit and for an increasing relaxation parameter value (from $\gamma = 0.01$ to $\gamma = 1$), we solved the blood flow problem starting from the same 20 initial tube hematocrit distributions. We constructed each one of these initial tube hematocrit distributions by sampling the hematocrit of each segment (excluding inlets) from a uniform distribution so that $H_{t,\text{initial}} \sim \mathscr{U}(0,1)$. Such a screening procedure can be seen as a very crude numerical continuation method[2].

To make sure that this screening procedure was capable of capturing different equilibria, we applied it first in ladder-like networks (Figure SI1), similar in topology to the hexagonal network depicted in Figure 2, but with an increased number of inlets and outlets. These networks were prescribed with uniform tube hematocrit at the inlets (red segments in Fig. SI1a) and uniform pressure drops between inlets and outlets (blue lines in Figure SI1a). Given their geometries and the boundary conditions prescribed, such networks always exhibit at least one trivial equilibrium regardless of the inlet tube hematocrit, which is no flow in horizontal segments and uniform flow and tube hematocrit in the vertical segments. Figure SI1b, which displays the tube hematocrit in the horizontal segment highlighted by a black arrow in Fig. SI1a, shows that in ladder networks, beyond a certain inlet tube hematocrit, this trivial equilibrium becomes unstable and more equilibria start to emerge. We note that this threshold is a decreasing function of the network size so that the trivial equilibrium, in large network, starts to destabilize for lower initial tube hematocrits. For ladder networks with the same size as the hexagonal network, we found that this threshold lies around $H_{t,\text{inlet}} \approx 0.8 \pm 0.05$, which is considerably larger than the range of inlet tube hematocrit explored experimentally in this work. Finally, we note that similar destabilizations were already obtained using a Wheatstone bridge-like network, with even the emergence of oscillations[3]. This shows that our screening procedure was able to capture, to some extent, different equilibria.

We repeated this procedure on the hexagonal network and the method did not converge towards more than one equilibrium, regardless of the inlet tube hematocrit considered. This does not definitely rule out the existence of several equilibria associated with the hexagonal network at low inlet tube hematocrit, however it strongly suggests that if they exist, such solutions are likely to be very close to each other and therefore cannot explain the difference observed between experiments and simulations in Fig. 3a.

SIB. Supplementary results: Tissue Fåhraeus effect

The tissue Fåhraeus effect (TFE) denotes a reduction of the volume fraction of RBCs in the whole network by comparison to its

---

Institut de Mécanique des Fluides de Toulouse, IMFT, Université de Toulouse, CNRS, Toulouse, France

‡ These authors contributed equally to this work

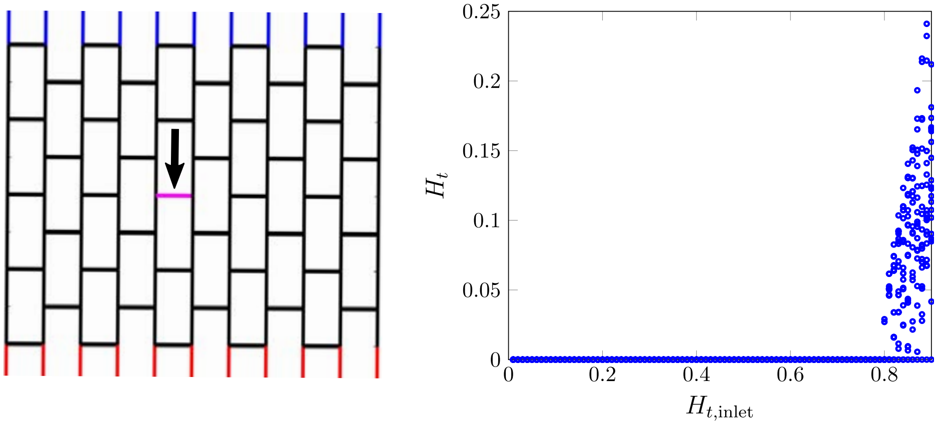

(a) (b)

Figure SI1 Multiple equilibria in a ladder network ($W = 10\mu m$). (a) Ladder network with inlets highlighted in red and outlets in blue. (b) Tube hematocrit in the purple horizontal segment highlighted by the black arrow in (a) as a function of inlet hematocrit.

discharge hematocrit (defined as the ratio between the RBC flow and the total flow)[4,5]:

$$TFE = \frac{\mathscr{V}_{RBC}}{\mathscr{V}}\frac{1}{H_d^i} = \frac{\mathscr{V}_{RBC}}{\mathscr{V}}\frac{Q_{RBC}^i}{Q^i},$$

where $\mathscr{V}_{RBC}$ is the total volume of RBCs within the network ($\mathscr{V}_{RBC} = \sum_k H_{t,k}\pi L_k r_k^2$), $\mathscr{V}$ is the total volume of the network ($\mathscr{V} = \sum_k \pi L_k r_k^2$) and H_d^i, Q_{RBC}^i and Q^i are the discharge hematocrit, the flow rate of RBCs and the total flow rate at the network inlet, respectively. It is analogous to the Fåhraeus effect, {i.e.}, the reduction of the hematocrit within a single segment (tube hematocrit) by comparison to the discharge hematocrit ($FE_k = {}^{H_{t,k}}/_{H_{d,k}}$). The latter results from the correlation between hematocrit and velocity within a single vessel cross-section[4,6], which can be evidenced by rewriting the Fåhraeus effect as the ratio between the RBC average transit time and the total average transit time throughout this vessel. Similarly, the tissue Fåhraeus effect can be expressed as the ratio between the RBC average travel time and the total average travel time throughout the network, and thus results from the correlation between high velocity and high hematocrit vessels.

Fig. SI2 displays the tube hematocrit as a function of RBC velocity in each channel of the hexagonal network, as predicted by the equivalent fluid network model, without correcting phase separation at order-1 bifurcations (red circles) and after correcting phase separation at order-1 bifurcations, as described in Sections 2.4 and 2.5. Except for the channels with the highest velocities (i.e. inlet channel and daughter channels of the order-0 bifurcation), where it does not change the tube hematocrit, this correction increases the tube hematocrit in all channels with a normalized velocity larger than ~ 0.2 and decreases the tube hematocrit in all channels with a normalized velocity larger than ~ 0.05, thus increasing the correlation between high velocity and high hematocrit channels. This results in a $\sim 10\%$ reduction of the value of TFE, corresponding to an increase of the tissue Fåhraeus effect.

SIC. Supplementary Results: RBC distribution in the hexagonal network with narrow channels

Experiments in such networks are extremely difficult to perform because RBCs quickly clog some channels despite the treatment of our microfluidic devices with BSA to reduce RBC adhesion at walls. This prevented from getting stable flow fields and RBC distributions over sufficient periods of time to extract quantitative measures of both the flow rate and hematocrit throughout the network. However, because the strong confinement induces a fast relaxation of RBCs toward the channel center at each bifurcation, the RBC distribution can be deduced using the equivalent fluid model described in Section 6.2. Figure SI3 shows the

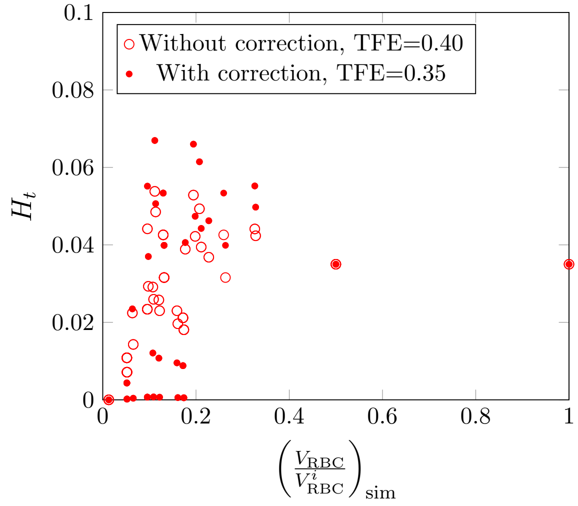

Figure SI2 Tube hematocrit as a function of red blood cell velocity in each segment of the hexagonal network, as predicted by the equivalent fluid network model, with (red dots) and without (red circles) correcting phase separation at order-1 bifurcations as described in Sections 2.4 and 2.5 ($W = 10\mu m$ and $H_t^i =$). For each scenario, the value of the tissue Fåhraeus effect is given in the legend.

corresponding simulated RBC distribution. Once again, the central region of the network is favored even if the heterogeneity at large scale is reduced compared to the simulation for large channels (see Fig. 7b for comparison). This same phenomenon arises when increasing the inlet tube hematocrit in the network with larger channels (simulations not shown).

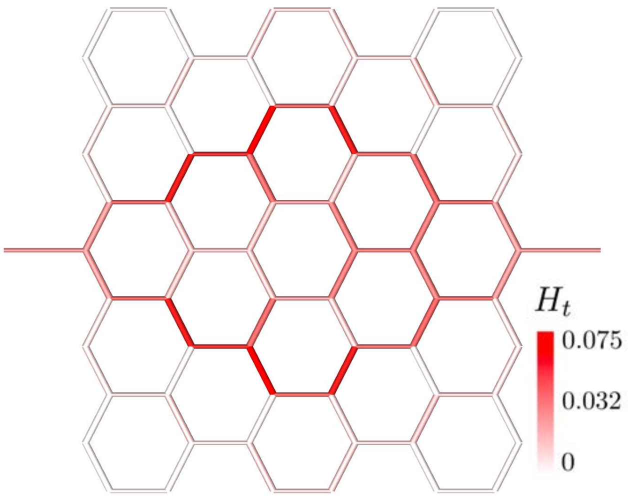

Figure SI3 Distribution of simulated tube hematocrit in a hexagonal network made of 5μm-wide channels with $H_t^i = 0.035$.

SID. Supplementary results: Structure of the baseline flow field in hexagonal and square networks

For flow in networks with channels of equal sizes, the structure of the baseline flow field can generally be inferred from the length of the flow pathways that connect the network inlet and outlet. For imposed inlet and outlet pressures, it is obvious that the pressure drop per unit length along a given pathway is inversely proportional to the length of this pathway, so that higher flow rates are expected on shorter pathways.

In the hexagonal network, the length of flow pathways that connect the network inlet and outlet is much shorter for pathways visiting the network center (see e.g. blue line in Fig. SI4, left panel), while they are longer for pathways visiting the network periphery (see e.g. orange trajectory in Fig. SI4, left panel). Thus, the pressure drop by unit length is smaller in the peripheral pathways compared to the central one, resulting in a smaller flow rate in branch β compared to branch α. Consistently, solving for the baseline flow field in this network yields $\frac{Q^\beta}{Q^\alpha} = 0.5803$ so that $\frac{l_{center}}{l_{periphery}} = 11/19 = 0.5789$ provides a good approximation for this flow ratio. A similar result would of course be obtained in a square network with a single inlet and outlet located in the center of opposite sides.

In the square network, however, the length of the peripheral pathways is equal to the length of the central ones (see e.g. orange vs. blue trajectory in Fig. SI4, right panel). As a result, the above rough approximation yields $\frac{Q^\beta}{Q^\alpha} = 1/2$, making it impossible to predict the branch with the highest flow. To go further, let consider the formal analogy between :

- the baseline pressure field in the square network, i.e. the solution of Eqs. 6 and 8 with uniform effective viscosity and imposed pressures ($P_i = 1$ and $P_o = 0$) at the inlet and outlet , respectively

- and the solution of the Laplace equation discretized with a finite-difference scheme over a square region with the following boundary conditions: imposed pressures at the lower-left and upper-right corner, and Neumann boundary-conditions ($\vec{\nabla} P.\vec{n} = 0$) everywhere else on the boundary.

Because isopressures and streamlines of the later are orthogonal to each other, we can deduce that isopressures are locally orthogonal to the domain boundaries, which are evident streamlines. Thus, the concavity of isopressures ($P \geq 0.5$) must be oriented toward the lower left corner, as schematized by the red dotted line in the right panel of Fig. SI4, and the concavity of isopressures ($P \leq 0.5$) must be oriented toward the upper right corner*. This yields a higher pressure drop, resulting in a larger flow rate, in branch β than in branch α.

SIE. Supplementary methods: Experiments

We compute the optical density profile OD(x) from the time-averaged grey-scale intensity profile $I(x)$ as follows[7–11]:

$$\mathrm{OD}(x) = -\log_{10}\left(\frac{I(x)}{I_{0(x)}}\right), \tag{SI.2}$$

where $I_0(x)$ is a reference intensity profile. Following Sherwood et al.[9], we assume that $I_0(x)$ is constant and equal to the grey-scale value in the PDMS far from any channel, as illustrated in Fig. SI3a. This is a reasonable approximation except in the close vicinity of the channel walls (see line transverse to the channel axis, where the channel is devoid of RBCs, highlighted in Fig. SI3a). Channel walls result in strong fluctuations of the intensity, with two bright stripes located outside the channel walls, resulting in peaks of high intensity as shown in Fig. SI3b. We assume these peaks are at equal distance to the channel center, and then determine the channel wall locations by translation ($\pm W/2$). Moreover, we discard the optical signatures of these channels walls, which appear in the time-averaged grey-scale intensity image (Fig. SI3c) and in the optical density profile, as shown by dotted lines in Fig. SI3d. More precisely, starting from the channel center, we only keep the positive optical density values, as in the left hand side of the channel, or the values encountered before the first local minimum, as in the right hand side of the channels. The hematocrit profile is then estimated as follows (Fig. SI3e): in the central region, it is deduced by calibration from the Optical Density value (see below); on the side where negative values of the Optical Density have been discarded, it is assumed to be null, on the side where a local minimum has been reached, it is inferred from the optical density profile by linear extrapolation.

We calibrated the relationship between the local optical density and the local depth-averaged hematocrit by using Leja slides (Leja Products B.V.). These are manufactured Hele-Shaw cells

---

* resulting in the isopressure line ($P = 0.5$) being the upper-left to lower-right diagonal.

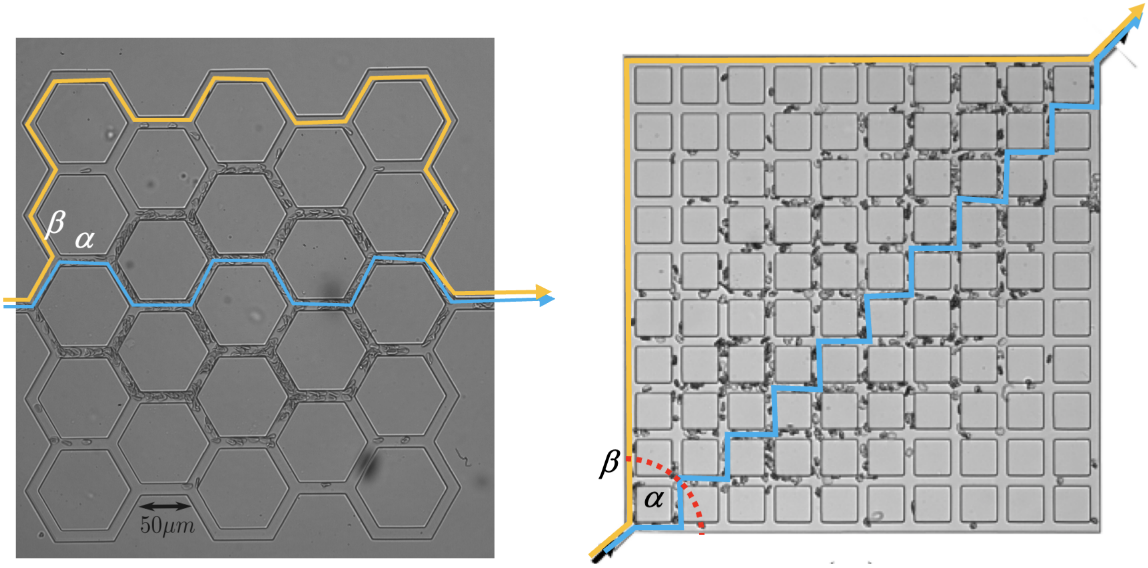

Figure SI4 Examples of central (blue) and peripheral (orange) trajectories in the hexagonal (left) and square (right) configuration. Consistent with the notations used in the manuscript, α denotes the daughter branch of order-1 bifurcations located on the same side than the previous, order-0, bifurcation apex. The red dotted line schematizes the isopressure line corresponding to α downstream vertex.

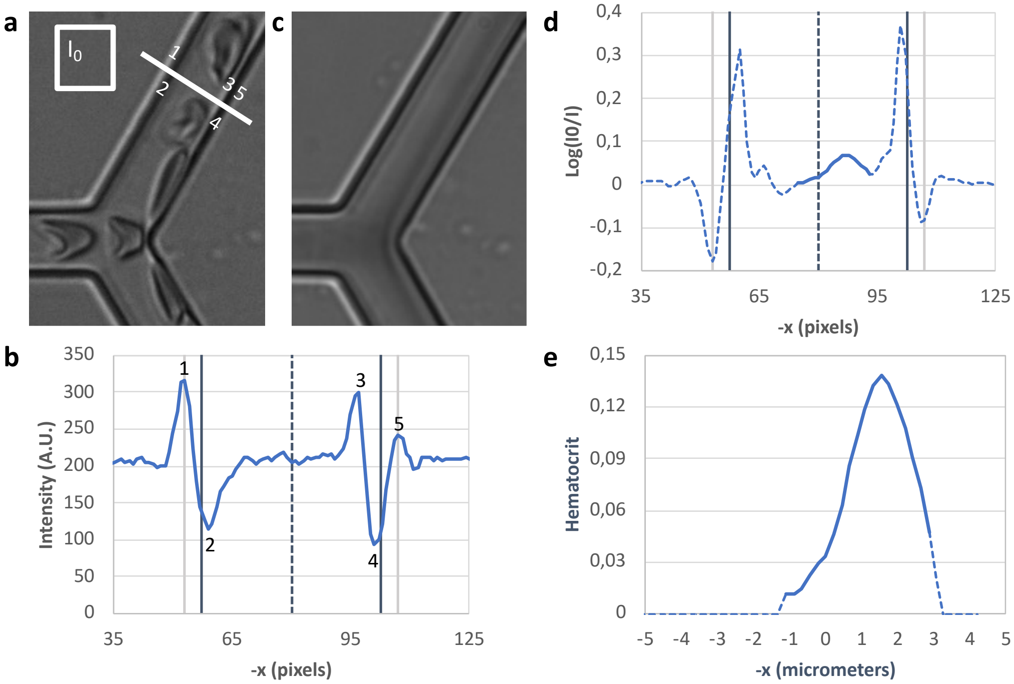

Figure SI5 Experimental determination of hematocrit profiles in channels with square cross-sections of $10 \times 10 \mu m^2$. a: Instantaneous snapshot showing a typical area used for estimating the average background intensity I_0 and a line transverse to the channel axis, where the channel is devoid of RBCs. Labels 1, 3 and 5 highlight the bright stripes induced by channel walls and labels 2 and 4 highlight the dark stripes; b: Instantaneous intensity profile (Arbitrary Units) associated to the transverse line highlighted in Panel a. The two outermost peaks (grey continuous lines) correspond to stripes 1 and 5 in Panel a, and are assumed to be at equal distance to the channel center (dashed line). Locations of the channel walls (black continuous lines) are deduced from the channel center by translation $(\pm W/2)$; c: Intensity I averaged over 3 seconds, keeping one of ten snapshots to avoid considering the same RBC multiple times at the same location. d. Optical Density (blue) profile on the same line as in Panel b, estimated as $Log(I/I_0)$. Dashed lines highlight the locations where the Optical Density is perturbed by the vessel walls, while the continuous line highlights the locations where we consider it is proportional to the hematocrit, according to the calibration displayed in Fig. SI4; e. Hematocrit, directly obtained from the measured Optical Density and the calibration curve shown in Fig. SI6 (continuous line) or inferred by linear interpolation and replacement of negative values by zero (dashed line).

with finely controlled depths (10 or 20μm) and much larger length and width ($\sim 2cm$). We filled each slide extremely slowly with a small volume of RBC suspension of known feed hematocrit, so as to reduce as much as possible local hematocrit heterogeneities within the slide, while ensuring it contained the whole injected volume. In that way, the local hematocrit is everywhere equal to the feed hematocrit, which enables precise calibration of the optical density, even for suspensions where RBCs are not individually discernible. As expected from Beer-Lambert law, the slope of the linear regressions obtained for moderate hematocrit values in 20μm Leja slides is twice the slope obtained in 10μm Leja slides. Also, the results obtained in the present work match those obtained previously in 20μm-side channels with the same imaging system, in the limit of small hematocrits, which validates the calibration method.

Finally, we derive the tube hematocrit H_t associated to each microchannel by averaging $H(x)$ over the channel width W at a longitudinal position in the channel where the RBC velocity profile is neither influenced by the previous nor by the next bifurcation ($z = 45\mu$m):

$$H_t = \left[\frac{1}{W}\int_{-W/2}^{W/2} H(x)dx\right]_{z=45\mu\text{m}}. \tag{SI.3}$$

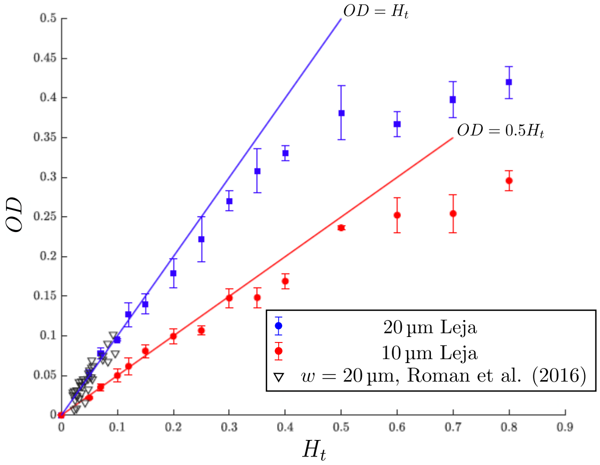

Figure SI6 Calibration of optical density from local depth-averaged hematocrit. Filled symbols: mean and standard deviation for 3 experiments in Leja Slides. Red circles: 10μm depth; Blue squares: 20μm depth. Empty triangles: data obtained by Roman et al.[10] in 20μm side channels for small hematocrits, which can be measured by individually counting the RBCs. Lines: linear regressions for H from 0 to 0.3 (10μm depth) or 0 to 0.15 (20μm depth).

SIF. Supplementary methods: Numerical solving of the blood flow problem

The blood flow model is defined by Eqs. 6-17 and represents a coupled non-linear problem that we solve iteratively. Each iteration is divided into two steps. First, we solve the linear system formed by Eqs. 6 and 8-11, which yields the pressure and total flow rate, using the discharge hematocrit obtained at the previous iteration, so that

$$\sum_j Q_{ij}^{n+1} = 0, \tag{SI.4}$$

$$Q_{ij}^{n+1} = \frac{\pi d_{\text{h},ij}^4}{128\mu_{\text{eff},ij}(H_{d,ij}^n)L_{ij}}\left(P_i^{n+1} - P_j^{n+1}\right), \tag{SI.5}$$

where $n+1$ represents the current iteration, n the previous iteration and where $\mu_{\text{eff},ij}(H_{d,ij}^n)$ highlights the dependency of the effective viscosity upon the unknowns of the problem. We then use the flow rate solution of the above two equations, to solve Eqs. 7, 12 and 13, which yields the discharge hematocrit so that

$$\sum_j H_{d,ij}^{n+1} Q_{ij}^{n+1} = 0, \tag{SI.6}$$

at all bifurcations and

$$H_{d,\alpha}^{n+1} = \frac{FQ_E^{\alpha}(H_{d,e}^n, FQ_B^{\alpha,n+1})}{FQ_B^{\alpha,n+1}} H_{d,e}^{n+1}, \tag{SI.7}$$

$$H_{d,\beta}^{n+1} = \frac{1 - FQ_E^{\alpha}(H_{d,e}^n, FQ_B^{\alpha,n+1})}{1 - FQ_B^{\alpha,n+1}} H_{d,e}^{n+1}, \tag{SI.8}$$

at each diverging bifurcations. We recall that $FQ_B^{\alpha,n+1} = \left|\frac{Q_\alpha^{n+1}}{Q_e^{n+1}}\right|$ and that $FQ_E^{\alpha}(H_{d,e}^n, FQ_B^{\alpha,n+1})$ is described by Eq. 14. We note that FQ_E^{α} uses the discharge hematocrit values at the previous iteration ($H_{d,e}^n$), so that Eqs. SI.6 to SI.8 also form a linear system straightforward to solve. This two-step method is justified since RBCs have a relatively weak feedback on the flow (*i.e.* $\frac{\partial \mu_{\text{eff},ij}}{\partial H_{d,ij}}$ is small), especially in the regime of small discharge hematocrit, which is the focus of this work, so that equation SI.5 can be linearized and truncated around $H_{d,ij}^n$.

References

1 N. J. Karst, J. B. Geddes and R. T. Carr, Bulletin of Mathematical Biology, 2017, **79**, 662–681.
2 E. L. Allgower and K. Georg, Numerical Continuation Methods, Springer, Berlin, Heidelberg, 1990.
3 N. J. Karst, B. D. Storey and J. B. Geddes, Bulletin of Mathematical Biology, 2015, **77**, 1377–1400.
4 A. R. Pries and P. Gaehtgens, in Dispersion of Blood Cell Flow in Microvascular Networks, ed. J.-S. Lee and T. C. Skalak, Springer New York, New York, NY, 1989, pp. 50–64.
5 A. R. Pries, T. W. Secomb and P. Gaehtgens, American Journal of Physiology-Heart and Circulatory Physiology, 1995, **269**, H1713–H1722.
6 A. R. Pries, T. W. Secomb and P. Gaehtgens, Cardiovascular Research, 1996, **32**, 654–667.
7 H. H. Lipowsky, S. Usami, S. Chien and R. N. Pittman, Microvascular Research, 1982, **24**, 42 – 55.
8 A. R. Pries, G. Kanzow and P. Gaehtgens, American Journal of Physiology-Heart and Circulatory Physiology, 1983, **245**, H167–H177.

9 J. M. Sherwood, E. Kaliviotis, J. Dusting and S. Balabani, Biomechanics and Modeling in Mechanobiology, 2014, **13**, 259–273.

10 S. Roman, A. Merlo, P. Duru, F. Risso and S. Lorthois, Biomicrofluidics, 2016, **10**, 034103.

11 A. Mantegazza, F. Clavica and D. Obrist, Biomicrofluidics, 2020, **14**, 014101.